SKOLKOVO INSTITUTE OF SCIENCE AND TECHNOLOGY

as a manuscript

Sergey Dyakov

Optical properties of resonant photonic structures in the visible and infrared ranges

Dissertation Summary

for the purpose of obtaining academic degree

Doctor of Science in Physics

Moscow - 2022

The dissertation was prepared at Skolkovo Institute of Science and Technology

Scientific Advisor: **Doctor of Science**, Prof. Nikolay Gippius, Skolkovo Institute of Science and Technology

General description of work

Relevance of the topic

Over the past three decades, the study of the interaction of radiation with matter has reached a new qualitative level due to the rapid development of the possibilities of controlled manufacturing of nano- and microstructures with the required shape and size. This opened up broad prospects for the creation of materials with unique optical properties, and also predetermined the main directions of research in solid state physics and optics for years to come.

In particular, the idea of creating a light source compatible with standard silicon technology, the basis of up-to-date nanoelectronics, has gained new momentum due to the ability to control the dielectric environment of semiconductor quantum dots. It is well known that a quantum dot placed in a highly inhomogeneous dielectric medium can exhibit optical properties that differ better from the optical properties of a quantum dot in free space in terms of photoluminescence intensity and its relaxation time. Therefore, the problem of searching for the dielectric environment of point light sources, to which a part of the dissertation is devoted, is certainly an important and urgent task of modern photonics. In addition, the inhomogeneous dielectric environment of emitting objects also makes it possible to control the direction of radiation with a given polarization state in various photonic structures, which is of interest to researchers, since such effects can be used not only in optoelectronics, but also in quantum information processing, biodetection, and optical filtration.

In parallel with research in the field of silicon photonics, the scientific community is also attracted by alternative platforms for nanoelectronics, such as plasmonics, polaritonics, graphene electronics, metasurface photonics, etc. The advantage of plasmonics over traditional semiconductor photonics is the ability of nanoplasmonic systems to localize light on a much smaller scale, which looks very attractive from the point of view of implementing optical communication between chip elements and between adjacent chips.

One of the promising ways to control the optical properties of dielectric and plasmonic nanosystems is the use of magneto-optical effects in materials with magnetic nanostructures. Such structures are currently attracting much attention, since they represent the basis of the potential of magneto-optical effects for data storage, for use in optical isolation systems, in various magnetic and biological sensors. Magneto-optical effects can also be used to implement ultrafast optical switches in nanophotonic circuits, where short RF or optical pulses are used instead of a slowly varying external magnetic field to control the dynamics of magnetization in magnetic media.

Another area of photonics that is interesting from both fundamental and applied points of view is the study of near-field radiative heat transfer in vacuum between different microstructures. As is known, as the distance between objects decreases down to submicron, the intensity of heat transfer between them increases by orders of magnitude compared with the case of far-field radiative heat transfer. Such giant amplification can be used to fabricate micro- and nanostructures with artificially created thermal conductivity, which is of great interest for applications where it is necessary to effectively control heat, for example, in thermophotovoltaics.

All described promising systems and effects are the subject of this dissertation, which makes it **relevant**. Thus, the main topic of the dissertation is the study of the interaction of radiation with matter in dielectric and metal-dielectric nanostructures, including semiconductor photonic crystal layers and single nanoobjects.

Goals of this work is a theoretical study of the influence of the near-field redistribution of the field of resonant states of inhomogeneous nano- and micro-objects on their optical properties in the visible and infrared ranges, as well as the study of the possibility of creating new photonics and optoelectronics devices based on the revealed phenomena.

To achieve this goal, the following **objectives** are set and solved in the work:

1. to implement as programs an algorithm for calculating the optical properties of layer-by-layer periodic structures in the formalism of the Fourier-modal method in the scattering matrix form;
2. to investigate the effect of field redistribution on the optical properties of dielectric and metal-dielectric photonic crystal structures, such as the spectra of reflection, transmission, photoluminescence and the transverse magneto-optical Kerr effect;
3. to investigate the radiative characteristics of point light sources located in a dielectric two-dimensionally periodic waveguide in

terms of possibility of obtaining narrow resonance lines in their photoluminescence spectra;

4. to study the possibility of using two-dimensionally periodic waveguide layers with a chiral metasurface profile to create and control circularly polarized radiation in the near and mid-infrared range;
5. to study the effect of eigenmodes of layered structures, metasurfaces and single nanoobjects on the Purcell factor of electric dipoles located in them;
6. to investigate the near-field radiative heat transfer between homogeneous plates of polar materials in static and dynamic cases.

Key provisions submitted for defense:

1. The appearance of quasiguided modes in magnetoplasmonic crystals with magnetite covered with a periodic array of gold nanostripes leads to a wideband enhancement of the magneto-optical Kerr effect in transmission compared to the case of homogeneous magnetite without gold nanostripes.
2. In wedge-shaped semiconductor structures, the Purcell factor of quantum dots located in them essentially depends on the thickness of the buffer layer separating the emitting layer from the substrate. This fact allows us to find the radiative and nonradiative recombination rates of these quantum dots, as well as their internal quantum efficiency.
3. The resonant redistribution of the field in gold nanorods coated with a thin layer of porous silicon dioxide leads to an increase in the Purcell factor of light emitters located near this system, as well as to the existence of optimal geometric parameters of this system in terms of photoluminescence intensity.
4. In a dielectric photonic crystal slab with emitting quantum dots, photoluminescence spectra contain high-Q peaks which are associated with symmetry-protected bound states in the continuum. In a hexagonal photonic crystal lattice, not only singlet, but also doublet bound states in the continuum can be used to obtain high-quality peaks in the photoluminescence spectra.

5. The resonant redistribution of the field in a double chiral photonic crystal slab waveguide leads to the effect of ideal vertical routing of radiation from a circularly polarized dipole located in it.
6. The resonant redistribution of the field in a chiral photonic crystal slab waveguide at infrared wavelengths leads to the effect of circularly polarized thermal radiation of such a structure with a high degree of circular polarization.
7. The intensity of near-field radiative heat transfer between two homogeneous parallel plates, the time of their thermalization, as well as their equilibrium temperatures essentially depend on the thickness of the plates and the distance between them.
8. In a system of homogeneous parallel plates of silicon dioxide and vanadium dioxide, which are in vacuum and exchange thermal energy by radiation, the first-order phase transition in vanadium dioxide leads to the appearance of thermal bistability and thermal self-oscillations when an external energy source is applied.

Scientific value and novelty of the work lies in the fact that it systematically studies the features of the light-matter interaction in the most complex case of structures with a characteristic size comparable with the wavelength of light in the visible, near infrared and mid infrared ranges. As a result of the work, a number of new effects, systems and phenomena that have not been previously studied and not mentioned in the literature, have been revealed, namely:

- for the first time, multiple wideband amplification of the transverse magneto-optical Kerr effect in magnetoplasmonic structures with magnetite, the most common magnetic material on Earth, has been demonstrated and comprehensively studied;
- for the first time, it has been demonstrated and comprehensively studied the enhancement of spontaneous emission of germanium quantum dots in a silicon photonic crystal slab waveguide with a hexagonal lattice, due to symmetry-protected bound states in the continuum;
- for the first time, an ideal vertical photon router based on a double chiral periodic crystal slab waveguide has been proposed and the principle of

its operation has been explained from the viewpoint of the structure symmetry;

- a chiral photonic crystal slab waveguide has been demonstrated for the first time, the thermal radiation of which is circularly polarized without an applied external magnetic field;
- The effects of near-field thermal bistability and thermal self-oscillations have been theoretically discovered in a system of parallel silicon dioxide and vanadium dioxide plates exchanging thermal energy in a radiative way.

Practical significance of the work lies in the fact that the results obtained can be used as fundamental physical effects that underlie future devices in photonics and optoelectronics.

Reliability of the results obtained in the work on the dissertation is confirmed by the repeatedly verified agreement between theoretical calculations and experimental data obtained in leading Russian and foreign scientific centers.

Approbation of work The results included in the dissertation work were reported and discussed at: "Nanophysics and nanoelectronics"symposiums (Nizhny Novgorod 2019, 2020 and 2021), international conferences on metamaterials and nanophotonics "Metanano"(St. Petersburg 2021, 2020, 2019, Sochi 2018), 14th all-Russian Conference on Semiconductor Physics (Novosibirsk 2019), International Conferences on Metamaterials, Photonic Crystals and Plasmonics "Meta"(Lisbon 2019, New York 2015), International Conference on Semiconductor Physics "ICPS"(Montpellier 2018), 2nd international symposium "Advanced research in chemistry and biomedicine"(Tomsk 2018), 26th international symposium "Nanostructures: physics and technology"(Minsk, 2018), 4th annual world congress "Smart materials"(Osaka 2018), Russian-French seminars on nanostructures and nanotechnologies (Suzdal 2017, Clermont-Ferrand 2019), international symposia on electromagnetism "PIERS"(St. Petersburg 2017, Shanghai 2016, Prague 2015, Guangzhou 2014), International Conferences of Electronic Materials Research Society "EMRS"(Warsaw 2017), 10th International Congress "Advanced Electromagnetic Materials in Microwaves and Optics"(Crete, 2016), Annual International Congress "Days of Diffraction"(St. Petersburg 2016), International Symposium SPIE "Optics + Optoelectronics"(Prague 2015), Annual International Conference "Optics and Photonics in Sweden"(Gothenburg, 2014), 4th International Conference on Advanced Research in Optoelectronics and Micro- and Nano-Optics "AOM"(Hangzhou 2014), International Conference "Micro+Nano Materials, Devices and Applications"(Melbourne 2013).

In addition, the results included in the dissertation work were reported and discussed at the Low-Dimensional Seminar (Ioffe Institute, St. Petersburg 2020), at the seminar of the scientific group of Prof. Min Chu (Zhejiang University, Hangzhou, China, 2014), as well as at the seminar of Prof. Minoru Fujii (Kobe University, Japan, 2018).

The main content of the work is presented in 15 first-tier publications [A1—A15] и 3 second-tier publications [B1—B3]. During the work on the dissertation, the author also published 28 articles on topics not included in the dissertation [C1—C28], and made 11 invited presentations at international conferences [D1—D11].

Contents

Introduction substantiates the relevance of research conducted within the framework of this dissertation work, formulates the goal, sets the objectives of the work, formulates the scientific novelty and practical significance of the presented work.

The **First chapter** is devoted to the description of theoretical methods for calculating the optical properties of nano- and microstructures, which are the object of study of this dissertation. In the introductory part, an overview of the main theoretical methods of computational electrodynamics is given, their advantages and disadvantages are analyzed.

The first section of the first chapter describes the Fourier-modal method in detail, a main computational tool used in research within the framework of the dissertation, and the second section briefly describes the boundary element method.

In the **second chapter**, the effect of the band structure of optical resonances on the optical properties of periodic waveguide and waveguide-plasmon structures is studied. In Section 2.1, the photoluminescent (PL) response of silicon nanocrystals in structures with gold nanostripes is studied. Interest in such a study is due to the fact that a quantum dot placed in a highly inhomogeneous dielectric medium can exhibit optical properties that are very different from the optical

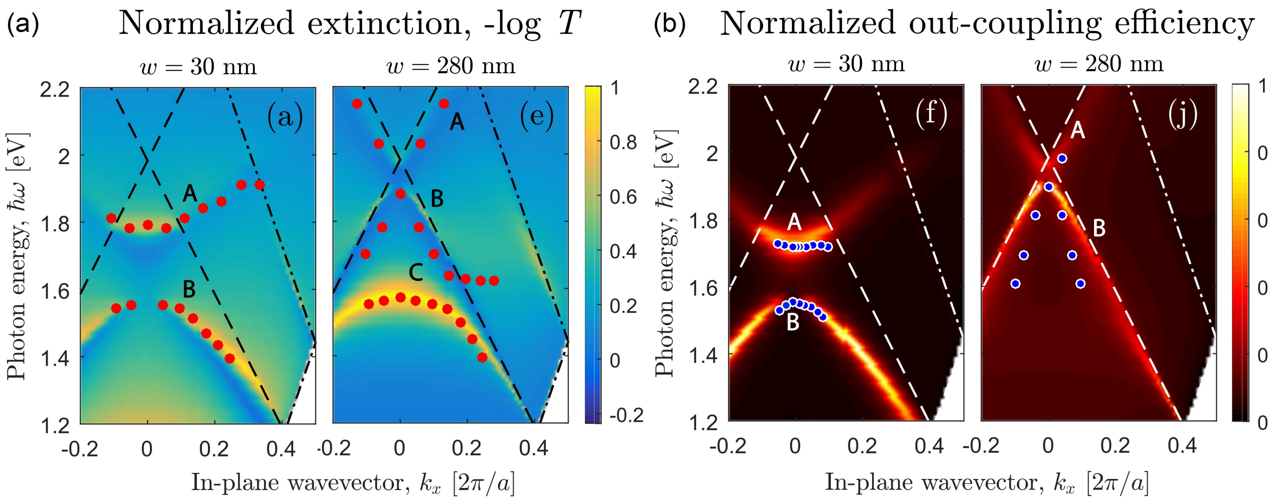

Fig. 1 — Calculated dependences of the extinction coefficient (a) and emissivity (b) on the wave vector and photon energy in TM polarization. The points on both graphs correspond to the peaks on the experimental spectra. From [A11].

properties of a quantum dot in free space [1]. From the optical point of view, in the approximation of a weak excitation and a sufficiently low nonradiative recombination rate, the intensity of the emission of a quantum dot into the far field is proportional to the product of the excitation efficiency and the far-field emissivity; the total PL intensity is given by summing the following products over all silicon nanocrystals:

$$I = \sum_i \left| \vec{E} \left(\hbar\omega_{\mathrm{exc}}, \boldsymbol{\kappa}_{\mathrm{exc}}, \boldsymbol{r}_i \right) \right|^2 \times \left| \vec{E} \left(\hbar\omega_{\mathrm{PL}}, \boldsymbol{\kappa}_{\mathrm{PL}}, \boldsymbol{r}_i \right) \right|^2 , \tag{1}$$

where $\vec{E}$ is the electric vector of the incident plane electromagnetic wave calculated at photon energies $\hbar\omega$ and the horizontal projection of the wave vector $\boldsymbol{\kappa}$ of excitation or PL in the emitter's coordinate $\mathbf{r}_i$. This section is devoted to studying the influence of optical resonances of metal-dielectric gratings on both of these factors.

The structure under study is an array of air gaps in a gold film 20 nm thick deposited on a quartz substrate coated with a thin SiO_2 film with silicon nanocrystals[1]. It is shown that the extinction and photoluminescence spectra have several families of peaks, which are attributed to surface plasmon polaritons,

---

[1] Samples with silicon nanocrystals were made in the group of prof. Margit Zacharias, University of Freiburg, Germany, gold stripes were applied by electron lithography by Alexander Marinin at the Royal Technical School, Stockholm, Sweden, measurements were carried out by Denis Zhigunov at the Faculty of Physics, Moscow State University.

localized surface plasmons, or quasiguided modes depending on the width of the air gap; the field distributions in these modes is plotted. A smooth transition between surface plasmon polaritons and localized plasmons is also shown with a change in the air gap width, w. The calculated dependencies of the extinction coefficient and emissivity in TM polarization on the wave vector and photon energy are shown in Fig. 1. On these dependencies, the C mode is a localized surface plasmon, which shifts to higher energies with increasing w and interacts with the lower quasi-waveguide mode B. Due to the strong coupling between the localized surface plasmon mode C and the quasiguided mode B, a hybrid waveguide plasmon-polariton mode [2] appears, leading to an increase in the PL intensity at the corresponding wavelengths. This hybrid mode has two branches B and C, the Rabi splitting between them is about 100. Finally, we analyzed how the position of the silicon nanocrystal in the structure affects its contribution to the overall PL intensity. It is shown that, in the surface plasmon-polariton regime, the main contribution to the PL intensity is made by near-surface silicon nanocrystals. In the waveguide mode, when the air gap is wide, the main contribution to the PL is made by silicon nanocrystals deep in the emitting layer. In both cases, the distribution of the contribution of silicon nanocrystals to the total PL intensity is highly inhomogeneous.

Section 2.2 is devoted to the reflection spectra of opaline photonic crystals coated with $Ge_2Sb_2Te_5$ (GST) layer. Opal is a form of amorphous silica composed of a periodic array of SiO_2 spherical beads. The optical properties of opals are largely determined by the configuration of its photonic crystal lattice, including its period, refractive index, and orientation. Natural opals have sphere diameters of the order of several hundred nanometers, so they have a photonic stop band in the visible spectral range of electromagnetic waves. Since the spectral position of the photon stop band depends on the viewing angle, noble opals are characterized by an iridescent overflow of colors — opalescence. The optical properties of opals can be effectively changed by mechanical deformation of the photonic crystal lattice [3; 4] or the shape of opal particles [4]. Another way to change the optical properties of an opal is to control the geometry and composition of its surface. The purpose of this section is to reveal the origin of Wood's anomalies in the optical reflection of opals coated with a material with a high refractive index, GST [5]. To this end, the eigenmodes are analyzed, the reflection spectra are modeled, and the

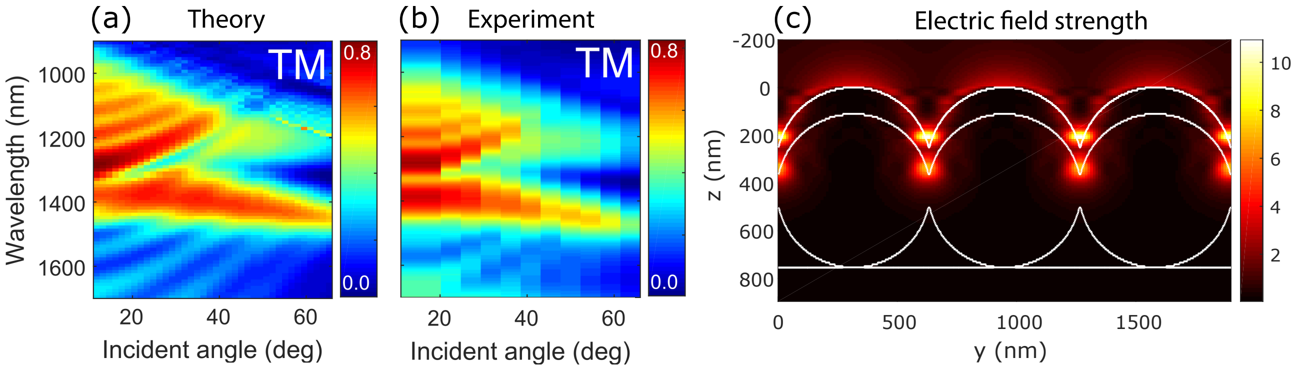

Fig. 2 — Theoretical (a) and experimental (b) reflection spectra of the photonic crystal GST225/opal structure depending on the angle of incidence in TM polarization. (c) Electric field of an incident electromagnetic wave at $\lambda = 1310$ nm, $\theta = 56°$ in TM polarization. The thickness of the cover layer GST225 for all panels is $h = 110$ nm.

distributions of the electromagnetic field in the near zone in opal structures are calculated.

Samples of the hybrid structures under study consist of 1 and 16 monolayers of amorphous silicon dioxide spheres with a diameter of ≈ 645 nm, grown[2] on a fused quartz substrate and coated with a GST225 film with a thickness of ≈ 110 nm. Theoretical and experimental reflection coefficients of the structures under study are shown in Fig. 2, from which it can be seen that there are two peaks in the spectra, which redshift with increasing angle of incidence. These peaks are Wood-Fano anomalies corresponding to two different quasiguided modes. The peak reflection coefficient increases monotonically with decreasing angle of incidence, reaching a maximum at normal incidence ($\theta = 0$). At very small angles θ, the Wood-Fano anomalies merge into a wide band. The dissertation shows that the reason for the appearance of quasiguided modes is the existence of a GST cover layer, the dielectric permittivity of which is greater than that of silicon dioxide. Fig. 2c shows the distribution of the electric field in such modes, from which it can be seen that it is mainly localized in the near-surface region in the gaps between the opal spheres. Finally, the experimental reflection spectrum of a single-layer opal structure is approximated by the Lorentz function corresponding to the Fano resonance, and its parameters are determined.

In Section 2.3, a transverse magneto-optical Kerr effect in structures with magnetite is studied. Magneto-optical effects in materials with magnetic

---

[2] The fabrication of opal samples and experimental measurements were carried out at the Ioffe Institute under the supervision of Prof. Alexander Borisovich Pevtsov.

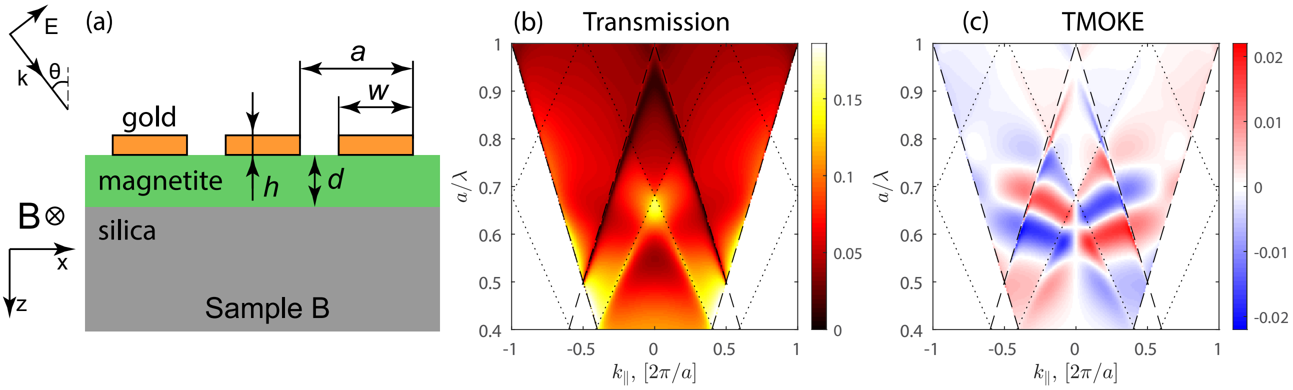

Fig. 3 — (a) Diagram of a magnetoplasmonic crystal. In all samples, the thickness of the magnetite film is $d = 100$ nm, the lattice period is $a = 580$ nm, and the width of the gold nanostripes is $w = 400$ nm. Calculated transmittance (b), and TMOKE (c) as a function of k_x and a/λ.

nanostructures are currently attracting much attention, since they allow one to control the intensity of reflected and transmitted light [6]. This is the basis of the potential of magneto-optical effects for data storage [7], for use in optical isolation systems [8], in various magnetic [9] and biological sensors [10], as well as in optical filtering [11]. Magneto-optical effects can also be used to implement ultrafast optical switches in nanophotonic circuits, where short RF or optical pulses are used instead of a slowly changing external magnetic field to control the magnetization dynamics in magnetic media [12]. In this section, we study magnetoplasmonic crystals consisting of a magnetite film with arrays of gold nanostripes[3]. The great interest in the TMOKE effect in magnetite is due to the fact that this material is the most magnetic of all natural minerals on Earth.

The optical properties of magnetized magnetite are macroscopically described by the off-diagonal permittivity tensor, which in the linear approximation for the magnetization has the form:

$$\hat{\varepsilon} = \begin{bmatrix} \varepsilon & -ig_z & ig_y \\ ig_z & \varepsilon & -ig_x \\ -ig_y & ig_x & \varepsilon \end{bmatrix}, \tag{2}$$

where ε is the permittivity of magnetite in the absence of magnetization. All diagonal components of the permittivity tensor are equal, since there is

---

[3] Fabrication of samples with magnetite was done by Sergey Pavlov from Ioffe Institute, St. Petersburg, and measurements were carried out by Lars Klompmaker, Felix Spitzer and Ilia Akimov from the University of Dortmund, Germany.

no anisotropy in Fe_3O_4 nanocrystalline films. The complex gyration vector $\vec{g} = (g_x, g_y, g_z)$ is proportional to the magnetization $\vec{g} = \alpha\vec{M}$, where the proportionality factor α does not depend on the magnetization direction. In the dissertation, complex gyration was also determined by measuring the Faraday rotation and ellipticity of a homogeneous layer of magnetite on a SiO_2 substrate, when the direction of light propagation was parallel to the direction of the magnetic field and perpendicular to the plane of the layer, and the permittivity of magnetite was constructed according to the Drude-Lorentz model [13].

The resulting dependencies of the transmittance and TMOKE on $k_\parallel$ and a/λ are shown in Fig. 3b,c. Due to the high absorption in magnetite, the transmission spectra do not have sharp resonant peaks, which are usually observed for low-absorption periodic planar waveguides or magnetoplasmonic crystals as in the papers. At the same time, the TMOKE spectra are quite informative, since they show color changes (white bands), which can often, but not always, be associated with a specific resonance that is hardly visible in the transmission spectrum. The thesis shows that if some resonance at the frequency $\omega_0 - i\gamma$, described by the Lorentzian $L_0(\omega)$ which frequency changes the spectral position under the action of an external magnetic field by $\Delta\omega$, then the resulting signal TMOKE in this case takes the form

$$\delta = \frac{4\Delta\omega(\omega - \omega_0)L_0(\omega)}{I_0\gamma^2}, \tag{3}$$

This expression explains the sign change of TMOKE at the resonant frequency ω_0. Thus, TMOKE spectra generally provide better contrast for resonance observation than transmission spectra. The dissertation also describes the experimental demonstration of TMOKE amplification and shows that the obtained experimental data are well described by the theoretical model.

The **third chapter** is devoted to the influence of the symmetry of photonic crystal (PC) slabs on their radiative characteristics. Section 3.1 studies of bound states in the continuum (BIC) and the luminescence properties of PC layers with germanium quantum dots[4] (Fig. 4a). BICs are spatially localized states that are invisible from the air far field, despite the fact that their energy lies above the air

---

[4] All experimental data in this chapter were obtained by Margarita Vladimirovna Stepikhova, and the samples were made by Alexei Vitalievich Novikov from the Institute of Physics of Microstructures of the Russian Academy of Sciences, Nizhny Novgorod.

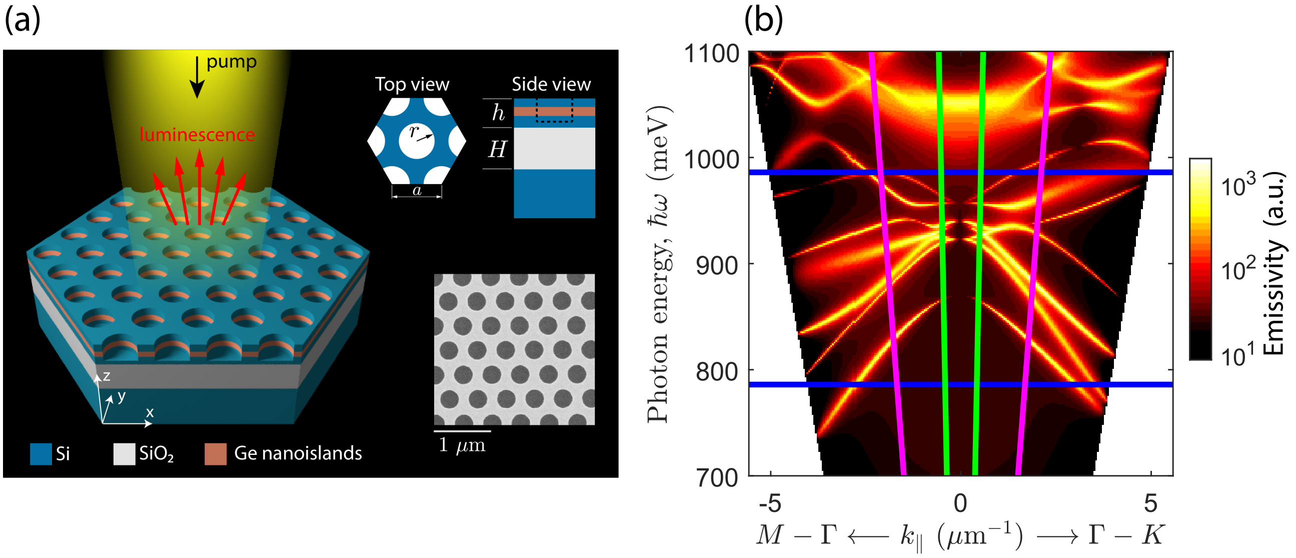

Fig. 4 — (a) Schematic of a photonic crystal slab (PCS) with 5 layers of Ge nanoislands. The insets show the top and side views of the PCS and the image of the PCS with air pores in the Si matrix obtained with a scanning electron microscope. (b) Dependence of the emissivity on the photon energy and in-plane wave vector, calculated for a grating with a = 570 nm and r/a = 0.26. The green and pink lines on the panel represent the light cones corresponding to the emisision angles $\alpha = 6^\circ$ and $\alpha = 25^\circ$, from which the light is collected in the two PL measurement methods described in the dissertation. Blue lines limit the energy range of intrinsic photoluminescence of Ge nanoislands. The color scale is logarithmic.

light cone. Essentially, the BICs arise due to destructive interference, when two or more waves are superimposed on each other, as a result of which radiation losses are completely suppressed. Because of this, their theoretical radiative lifetime tends to infinity. Despite the more than 20-year history of BICs, these resonances were mainly considered in vertically symmetric structures with a square FC lattice. Although hexagonal gratings are more commonly used to create high-Q photonic crystal cavities and to couple far-field to near-field [14—16], they have received much less attention from BIC researchers. In this work, we study the BIC-originated PL enhancement of self-organized Ge nanoislands embedded in a photonic crystal slab with a hexagonal lattice.

The calculated dependence of the PCS emissivity on the photon energy, $\hbar\omega$, and the horizontal projection of the wave vector, $k_{\parallel}$, is shown in Fig. 4b. The shown emissivity contains many resonances, which are quasiguided modes hybridized as a result of folding the waveguide modes of a homogeneous effective waveguide into the first Brillouin zone. It can be seen that some modes are doubly degenerate in the Γ point, i.e. are doublets, while outside the Γ-point the degeneracy is lifted.

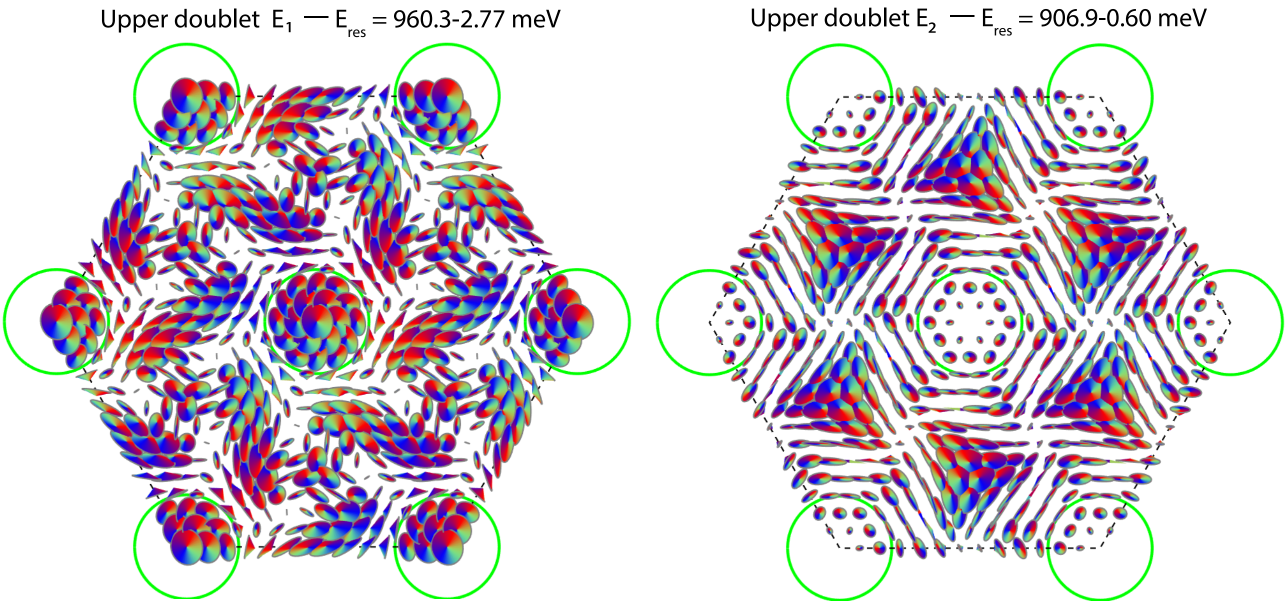
Upper doublet E_1 — E_{res} = 960.3-2.77 meV

Upper doublet E_2 — E_{res} = 906.9-0.60 meV

Fig. 5 — Phase representation of the electric field in the upper doublet E_1 and in the upper doublet E_2 for PCS with $a = 600$ nm and $r/a = 0.24$.

Group theory predicts that for a hexagonal C_{6v}-symmetric structure, there are four singlets and four first-order doublets in the Γ-point. Since all resonances have dispersion with $k_{\|}$, the resonance peaks that appear in the measured PL spectra are inhomogeneously broadened due to the nonzero numerical aperture of the collecting lens. In addition, the PL spectra have resonance peaks of different widths. As shown in the dissertation, the experimental quality factor of the peaks ranged from 150 to 2200.

In order to explain the differences between the quality factors of different resonances, the symmetry of the field of quasiguided modes was considered (an example is shown in Fig. 5). It can be seen from the figures presented in the dissertation that the intensity distributions in singlets are C_{6v} symmetric in accordance with the symmetry of the PCS. In the case of doublets, the intensity profile in eigenmodes cannot be C_{6v}-symmetric, but one can choose the basis of eigenfunctions so that the field intensities in them have C_6 symmetry. The distributions of E_z in singlets and doublets have a more complex symmetry. Group theory defines the symmetry of an eigenmode by a set of χ characters that characterize how the mode transforms under each symmetry operation in a point group.

Understanding the symmetry of modes is of direct practical importance. Namely, the symmetry type of the mode enables us to predict whether it can interact with the far field in the Γ point. The connection of the eigenmode with

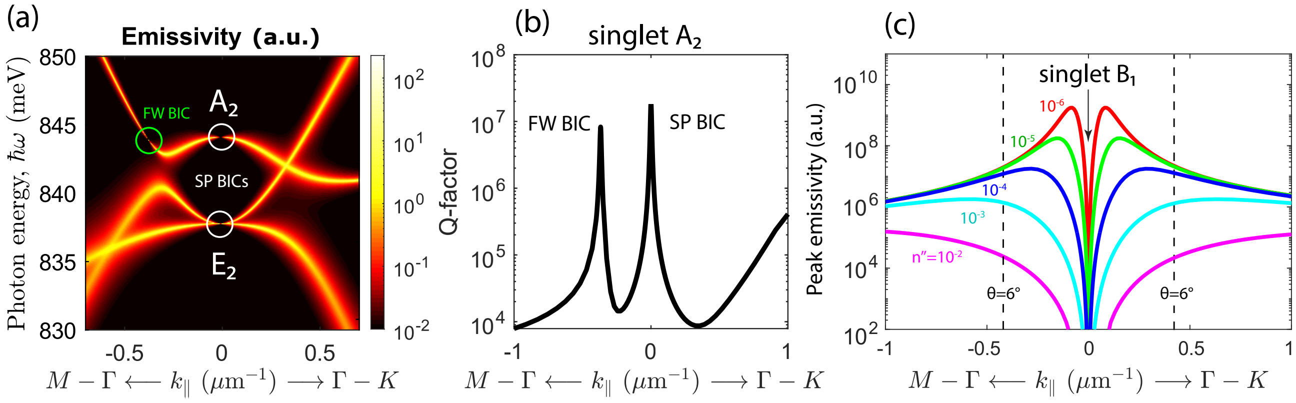

Fig. 6 — (a) Calculated dependence on the energy and wave vector of the photon emissivity near the Γ-point. Symmetry-protected (SM) and Friedrich-Wintgen (FW) BICs are distinguished.(b) Calculated figure of merit for the A_1 singlet near the Γ point. (c) Wave vector dependence of the emissivity peak calculated near the B_1 singlet for various imaginary parts of the complex refractive index n'' of the SiGe layer. PCS parameters: $a = 600\,\text{nm}$ and $r/a = 0.2$ and for panels (a) and (b) $n_{\text{eff}}(\text{SiGe}) = 3.12 + 10^{-6}i$.

free space is possible when the overlap integral γ is nonzero:

$$\gamma = \iint_{cell} \left(\vec{E}^*_{\text{fs}} \times \vec{H}_{\text{mode}} + \vec{E}^*_{\text{mode}} \times \vec{H}_{\text{fs}} \right) \text{d}S, \tag{4}$$

where dS is the area element of the photonic crystal unit cell, the indices fs and *mode* denote electric and magnetic fields in free space and in mode. Analyzing the characters of the irreducible representations of the point group C_{6v}, we can conclude that in the C_{6v}-symmetric hexagonal lattice, only the doublet E_1 is open for coupling with the far field, whereas all the singlets and the doublet E_2 are closed. Such closed modes are referred to as *symmetry-protected bound states in the continuum* [17; 18]. The emissivity of quantum dots at the frequencies of these modes in the Γ-dot is suppressed. It can be seen from Fig. 6b that there is one more point in k-space besides Γ where the emissivity is suppressed, and the resonance has zero width, namely $k_{\parallel} = 0.4\,\mu\text{m}^{-1}$ along the Γ-M direction. This is a bound state in the continuum of Friedrich-Wintgen type [19], which is the result of destructive interference between modes with similar radiation patterns in the far field [20].

Since the PCS emissivity in the Γ point is strictly equals to zero, the possibility of observing BIC-related peaks in the PL spectra depends on the power of Ohmic losses and the solid angle into which the PL signal is collected. In order to demonstrate this, we calculated the dependence on the horizontal

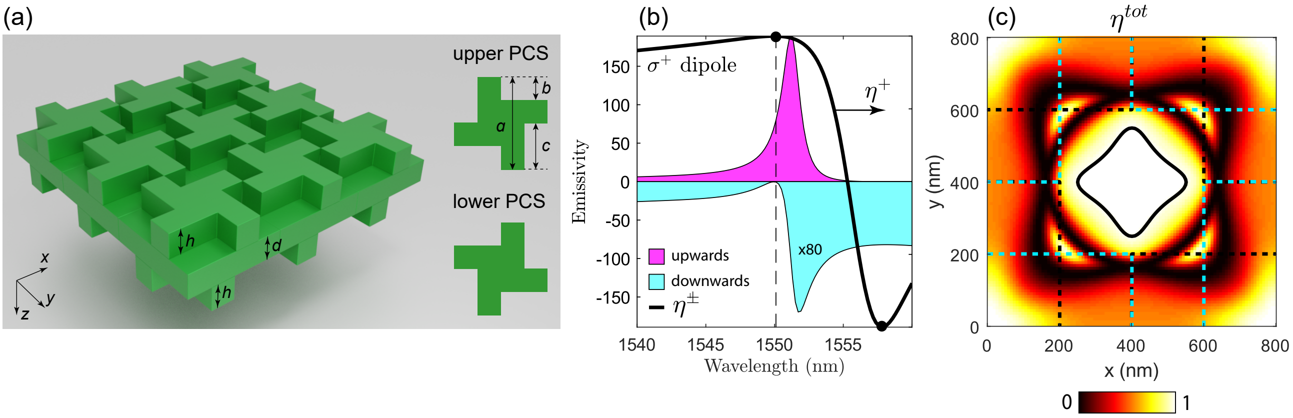

Fig. 7 — (a) Schematic of silicon structure with chiral PCSs with parameters: $a = 801$ nm, $b = a/4$, $c = a/2$, $h = 686$ nm, $d = 401$ nm, as well as elementary cells of the upper and lower PCSs. (b) Normalized upward (pink area) and downward (blue area) emissivities of the σ^+ dipole. The black line shows the corresponding routing efficiencies $\eta^\pm$. (c) Dependence of the total routing efficiency on the position of the σ^+ dipole on the xy-plane passing through the center of the cell. The blue and black dotted lines on the panels show the material boundaries in the upper and lower PCSs.

projection of the wave vector of the maximum emissivity near the singlet B_1 for various parameters n'', simulating Ohmic losses [21] under the assumption of a fixed density of Ge nanoislands (Fig. 6a). It is noteworthy that as long as the absorption losses are small ($n'' \leqslant 0.01$), the maximum peak emissivity is approximately inversely proportional to n''. Therefore, even at relatively high absorption (for example, $n'' = 10^{-2}$), the peak PL becomes measurable provided that the PL signal is collected far enough away from the Γ point. With high absorption, however, the quality factor of the resonance will be lower. Thus, to obtain resonant peaks with a high quality factor, one can use the advantage of BICs in lossless PC layers.

Section 3.2 presents the concept of an ideal vertical radiation router for dipoles located inside a D_4-symmetric structure, which is a silicon membrane with chiral morphology (Fig. 7a). It consists of a homogeneous plate located between two photonic crystal slabs mirror-symmetrical to each other with respect to the vertical plane. The calculated normalized emissivity spectra of σ^+ dipoles in the center of the unit cell of an optimized chiral metamembrane in the vertical upward and downward directions are shown in Fig. 7b. It can be seen that at a wavelength of 1550 nm, the emissivity in one of the directions is completely suppressed, which is explained by the Fano effect.

This asymmetry is described quantitatively using the routing efficiency η^+ and η^-, and the total routing efficiency η^{tot} as

$$\eta^{\pm} = \frac{I_{\mathrm{u}}^{\pm} - I_{\mathrm{d}}^{\pm}}{I_{\mathrm{u}}^{\pm} + I_{\mathrm{d}}^{\pm}}, \qquad \eta^{\mathrm{tot}} = -\eta^+\eta^-. \tag{5}$$

For practical implementation, it is of interest to study the stability of this effect with respect to the position of the dipole. The dependence of the upward emissivity on the position of the dipole in the horizontal plane passing through the center of the unit cell is shown in Fig. 7c. It can be seen that this dependence has a maximum in the central part of the cell. The dissertation also shows that efficient routing is possible for dipoles located in a sufficiently large unit cell volume. If a quantum dot located in this volume undergoes a spin-polarized transition, its upward or downward emission will be strongly suppressed.

In this work, as a demonstration of the possibility of routing the radiation of rotating dipoles, we use a structure with rotational symmetry D_4. Let us now show that the D_4 symmetry is more suitable for the ideal routing effect than the C_4 symmetry, which is often used to obtain circular dichroism. The structure shown in Fig.7a would have C_4 symmetry if it were on a substrate or if it had only one of the chiral PCSs. Let us consider the electric field below and above the membrane, created by an oscillating dipole located in the middle of the cell in the xy plane with an arbitrary coordinate z. Let us denote the complex components of the electric field created by the x-polarized dipole moment as $\vec{E}_{\mathrm{u}}^{x} = [\alpha, \beta]$ and $\vec{E}_{\mathrm{d}}^{x} = [\rho, \tau]$. Then for structures with C_4 symmetry, the fields generated by the y-polarized dipole moment will have the form: $\vec{E}_{\mathrm{u}}^{y} = [-\beta, \alpha]$ and $\vec{E}_{\mathrm{d}}^{y} = [-\tau, \rho]$.

According to the superposition principle, the electric fields from σ^+ and σ^- polarized dipoles are found as

$$\vec{E}_{\mathrm{u}}^{\sigma^{\pm}} = \vec{E}_{\mathrm{u}}^{x} \pm i\vec{E}_{\mathrm{u}}^{y} = (\alpha \mp i\beta)\,[1, \pm\, i] \tag{6}$$
$$\vec{E}_{\mathrm{d}}^{\sigma^{\pm}} = \vec{E}_{\mathrm{d}}^{x} \pm i\vec{E}_{\mathrm{d}}^{y} = (\rho \mp i\tau)\,[1, \pm i]\,. \tag{7}$$

When the two conditions $\alpha = -i\beta$ and $\rho = i\tau$ are met simultaneously, the radiation intensities of σ^+ dipoles downward and σ^- upward dipoles are equal to zero, and the resulting overall routing coefficient $\eta^{\mathrm{tot}} = 1$. The electric field components α, β, ρ, τ depend on the geometric parameters of the metamembrane,

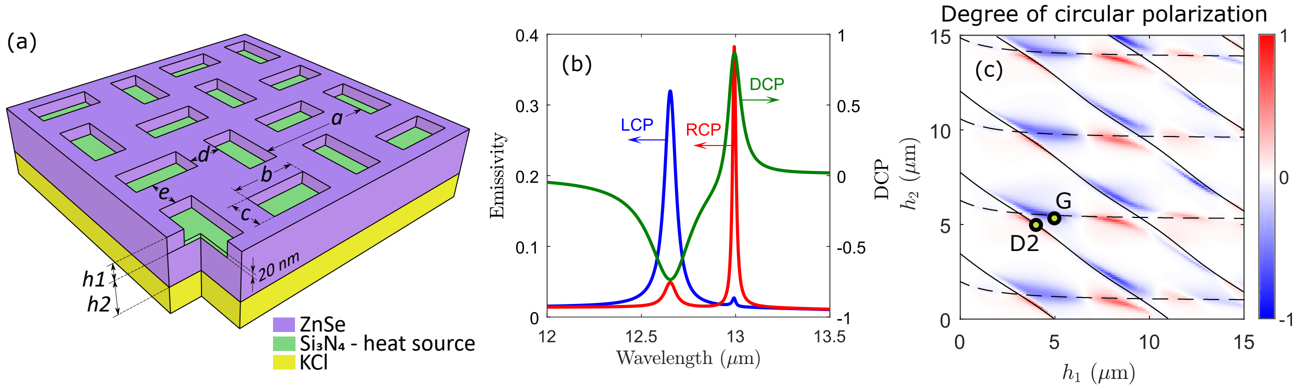

Fig. 8 — (a) Schematic representation of a chiral metasurface with parameters $a = 10$ μm, $b = 2a/5$, $c = a/5$. (b) Left and right circularly polarized emissivity spectra of a chiral metasurface with $h_1 = 4$ μm and $h_2 = 5$ μm. The degree of circular polarization is shown in green. (c) Degree of circular polarization as a function of thicknesses h_1 and h_2 at $\lambda = 13$ μm. Resonances in the empty lattice approximation are shown by dotted lines for TE polarization and thin solid lines for TM polarization.

and the simultaneous fulfillment of the above two conditions in structures with C_4 symmetry can be problematic. At the same time, structures with D_4 symmetry have another symmetry operation under which the structure is invariant, namely, a rotation by 180° about the y axis (or the x axis, which is equivalent). This leads to the fact that a dipole located at the center of a cell of any structure with D_4 symmetry generates an electric field such that $\rho = \alpha$ and $\tau = -\beta$. This makes the above conditions equivalent to each other. Thus, for structures with D_4 symmetry, the ideal routing condition is expressed by only one equality $\alpha = -i\beta$, which is much easier to satisfy than both of the above equalities at the same time.

Section 3.3 considers a source of circularly polarized thermal radiation based on a chiral PCS. In general, a system that does not have mirror symmetry can generate thermal radiation with circular polarization. Mirror symmetry can be broken, for example, by applying an external magnetic field due to the spin-orbit interaction of electrons [22]. This phenomenon is known as the magneto-optical Kerr effect; it explains, for example, the strong circular polarization of radiation from white dwarf stars [23]. Thermal radiation with circular polarization in a magnetic field was also observed in the [24] laboratory. Another way to break the mirror symmetry of a structure is to etch a pattern with chiral morphology on its surface. Metasurfaces with C_4 symmetry can have circular dichroism in transmission along the normal due to the absence of additional mirror symmetry about the plane parallel or perpendicular to the z-axis [25]. C_4-symmetric metasurfaces were used, for example, in [26; 27] to obtain circularly polarized PL spectra in the visible and near-IR ranges. The degree of circular polarization depends on the geometric parameters of the metasurface and is the subject of theoretical optimization. The highest obtained degree of circular polarization in optimized chiral structures was close to 100%. Due to the scalability of optical resonances, the operating range of C_4 symmetric structures can be shifted to the mid-infrared range by increasing their spatial period, which allows them to be used to control the polarization of thermal radiation.

The chiral source of thermal radiation (Fig. 8a) consists of a KCl substrate and a ZnSe waveguide with a two-dimensional array of etched rectangles. The etched pattern has a chiral morphology with C_4 rotational symmetry. The lower surface of the rectangles is covered with a Si_3N_4 layer 20 nm thick. In this work, we assume that the temperature of the heat source is close to 300 K and, therefore, we consider the wavelength range 7–15 μm. The choice of ZnSe and KCl materials is due to the fact that they are transparent in the mid-infrared range and therefore do not contribute to thermal radiation in this spectral range. On the contrary, Si_3N_4 has a wide absorption band and, therefore, is the only source of thermal radiation in the structure.

To evaluate the ability of the described chiral heat source to emit circularly polarized thermal radiation, we calculate its emissivity spectra in left-hand circular polarization (LCP) I_{LCP} and right-hand circular polarization (RCP) I_{RCP}, as well as the degree of circular polarization (DCP) as $\rho_c = (I_{\mathrm{RCP}} - I_{\mathrm{LCP}})/(I_{\mathrm{RCP}} + I_{\mathrm{LCP}})$. As shown in Fig. 8a, in the considered spectral range, the emissivity is characterized by two peaks, each of which has different amplitudes in the right and left circular polarization. As a result, the degree of circular polarization is not equal to zero and reaches -0.73 and 0.87 at $\lambda = 12.65$ and 13 μm, respectively. The dissertation shows that these peaks are quasiguided modes of the chiral PC layer and can be approximately described in the empty lattice approximation.

The degree of circular polarization of thermal radiation at $\lambda = 13\,\mu$m as a function of the thicknesses of the modulated and unmodulated parts of the chiral emitter, h_1 and h_2, is shown in Fig. 8c. It can be seen that the degree of circular polarization resonantly depends on the parameters h_1 and h_2, and one of the resonances does not depend on the thickness h_1. The reason for this is the fact that, in the structure under consideration, the TM modes are localized over the entire thickness of the PC layer, while the TE modes are localized only on its nonperiodic part. This mode behavior is explained using the effective medium theory: it turns out that for an effective anisotropic waveguide approximating a chiral PC layer, the waveguide mode in the TM polarization lies above the light cone of the uniaxial homogeneous medium, while in the TE polarization it lies below.

In addition, the dissertation discusses the Stokes parameters of the thermal radiation of a chiral PCS, and also shows its angular radiation pattern.

In the **fourth chapter** the Purcell effect in nanostructures with quantum dots is considered. Section 4.1 provides a definition of the Purcell factor and methods for calculating it. It is shown that for arbitrary-shaped structures, the Purcell factor can be found as the ratio of the total power dissipated by a dipole emitter in an inhomogeneous dielectric medium to the power of the same emitter in vacuum:

$$f(\omega) = \frac{P^{\text{cav}}(\omega)}{P(\omega)} \tag{8}$$

where

$$P^{\text{cav}}(\omega) = \oiint \vec{S}(\omega)\mathrm{d}\vec{A}, \qquad P(\omega) = \frac{|\vec{j}_0|^2\omega^2 n}{3c^3}. \tag{9}$$

In the case of layer-homogeneous and layer-periodic structures, integration over a closed surface in formula (9) can be replaced by finding the algebraic sum of the powers radiated vertically upward and downward by the dipole. This sum can be found by integrating in the momentum space. The resulting formula for calculating the Purcell factor for layered structures becomes:

$$F_p(\omega) = \frac{3c^3}{|j_0|^2\omega^2 n} \iint\limits_{-\infty}^{\infty} \left[\mathrm{S}_z^+(\omega,k_x,k_y) + \mathrm{S}_z^-(\omega,k_x,k_y)\right] dk_x dk_y, \tag{10}$$

where $\mathrm{S}_z^\pm(\omega,k_x,k_y) \equiv \mathrm{S}_z^+(\omega,k_x,k_y,z_d \pm 0)$. In two-dimensionally periodic layers, the integration is performed over the first Brillouin zone, and in calculating $\mathrm{S}_z^\pm$, the summation is performed over all Fourier harmonics.

In Section 4.2, radiative and nonradiative recombination rates, as well as the internal quantum efficiency of silicon quantum dots in a wedge-shaped structure, are determined for different radiation wavelength and temperatures by calculating the Purcell factor. By definition, the internal quantum efficiency is the

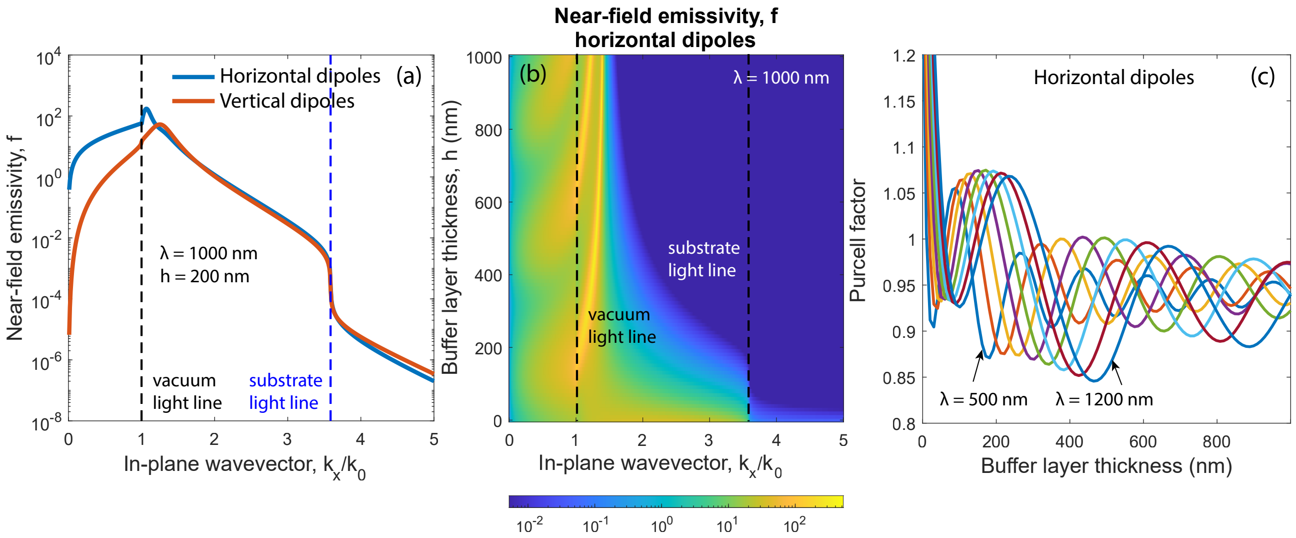

Fig. 9 — -field emissivity of silicon nanocrystals as a function of (a) the x-component of the wave vector and (b) the x-component of the wave vector and the thickness of the buffer layer, as well as the corresponding Purcell factors (c). The calculations were performed for randomly oriented horizontal dipoles. The dotted lines in panels (a,b) indicate the vacuum and silicon substrate light lines.

ratio of radiative recombination rate to the total recombination rate:

$$\eta = \frac{\Gamma_r}{\Gamma_r + \Gamma_{nr}}. \tag{11}$$

To determine the internal quantum efficiency from experimental data, we assume that Γ_r and Γ_{nr} do not depend on the spatial position of the emitter, while the Purcell factor does. This determines the geometry of the sample with nanocrystals — a wedge-shaped structure consisting of a thin layer with silicon nanocrystals in a silicon dioxide matrix (with a thickness of 22.5 nm) deposited on a wedge-shaped buffer layer, the thickness of which varies from point to point. To compare the position of points on the fabricated wedge-shaped sample with certain buffer layer thicknesses, the theoretical and experimental structure color profiles, as well as reflection and emission spectra are compared; based on good agreement between the calculated and measured data, one can conclude about the correctness of the model used.

The calculated near-field emissivities of silicon nanocrystals and the values of the Purcell factor for different wavelengths, wave vectors, and buffer layer thicknesses are shown in Fig. 9. It can be seen from Fig. 9, that for each buffer

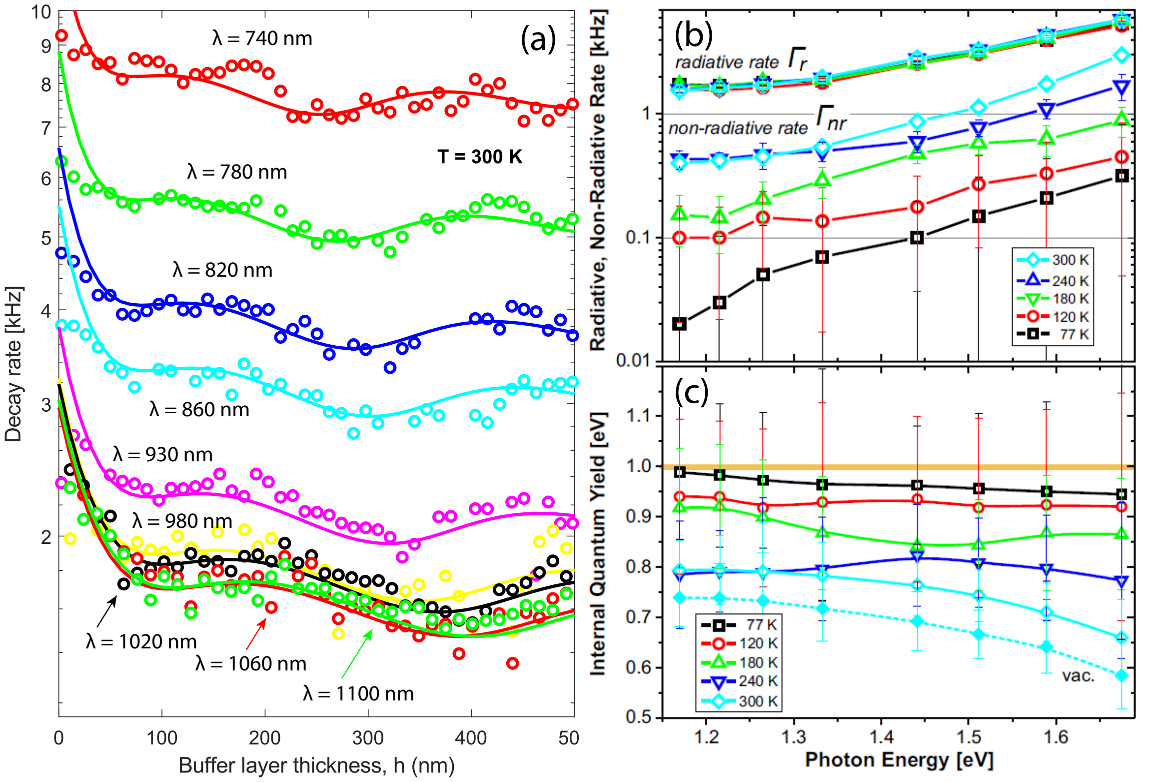

Fig. 10 — (a) Experimental dependencies of the spontaneous emission rate on the buffer layer thickness, $\Gamma^{\exp}(h)$, and the corresponding theoretical curves obtained as a result of interpolation using the formula (12). (b) Radiative and nonradiative recombination rates as a function of radiation wavelength and temperature. (c) Internal quantum efficiency calculated from the rates presented in panel (a). From [A9].

layer thickness, the maximum of the near-field emissivity is under the vacuum light cone; this means that the dipole mainly radiates into the substrate. In addition, the near-field emissivity also takes on nonzero, albeit rather small, values below the light cone of the substrate. Such a contribution to the Purcell factor is often referred to as PL quenching caused by evanescent surface waves due to nonzero absorption in the substrate. The undulation of the obtained functions of near-field emissivity and the Purcell factor is explained by Fabry-Perot resonances and waveguide modes on the thickness of the buffer layer.

Since at a given temperature the radiative and nonradiative recombination rates Γ_r and Γ_{nr} of silicon nanocrystals do not depend on the buffer layer thickness, the relation

$$\Gamma^{\exp}(h) = F_p(h)\Gamma_r + \Gamma_{nr}, \tag{12}$$

allows interpolating the experimental dependence of the recombination rate $\Gamma^{\exp}(h)$ and the theoretical function $F_p(h)$ using Γ_r and Γ_{nr} as fitting parameters.

This will enables us to determine these quantities as functions of temperature and radiation wavelength.

For this purpose[5], the time dependencies of the PL intensity of silicon nanocrystals (the decay kinetics) are measured, and from them the PL decay rates are determined. It can be seen from Fig. 10a that the decay rate dependencies on buffer layer thickness, in general, fit the theoretical curves quite well. The Γ_r and Γ_{nr} values determined for different PL wavelengths and temperatures, as well as the internal quantum efficiencies calculated from them using the formula (11), are shown in Fig. 10b,c. It can be seen from this figure that while nonradiative recombination rates increase strongly with temperature, radiative recombination rates are almost independent of it. Therefore, the internal quantum efficiency, obtained as the ratio of the radiative and total recombination rates, depends on temperature and decreases slightly towards shorter wavelengths. The highest internal quantum efficiency is found at a wavelength of 1000 nm (photon energy 1.2 eV): 74% at room temperature and almost 100% at 77 K.

Section 4.3 considers the lifetime and intensity of photoluminescence of silicon quantum dots near gold nanorods coated with a dielectric layer of some thickness. Despite the fact that, according to the electrodynamic reciprocity principle, the far-field emissivity of dipoles located near metal nanoparticles can take on very large values due to hotspots — localized plasmon resonances, the PL of molecules located too close to the metal surface can be strongly suppressed due to quenching. In order to describe such processes quantitatively, a two-level system of emitters was considered, and it was shown that the PL enhancement for such emitters compared to emitters in a homogeneous dielectric medium is equal to

$$\xi_{PL} = \frac{I_{\mathrm{PL}}}{I_{\mathrm{PL,o}}} = \frac{I_{\mathrm{exc}}}{I_{\mathrm{exc,o}}} \cdot \frac{F_p^{\mathrm{ext}}(\Gamma_{\mathrm{nr}} + \Gamma_{\mathrm{r}})}{\Gamma_{\mathrm{nr}} + F_p\Gamma_{\mathrm{r}}} = \xi_{\mathrm{exc}} \cdot \xi_{\mathrm{QY}}, \tag{13}$$

where ξ_{exc} is the excitation enhancement and ξ_{QY} is the external quantum yield enhancement, I_{exc} is the external excitation intensity, I_{PL} is the PL intensity, F_p is the Purcell factor, F_p^{ext} is the external part of the Purcell factor responsible only for radiation to the far field, and the symbol "o"means that the corresponding values are taken for emitters in a homogeneous medium. One can also introduce

---

[5] All measurements performed on the samples, including spectroscopic ellipsometry, time-resolved photoluminescence spectroscopy, were performed by Mikel Greben and Prof. Jan Valenta from Charles University, Prague, Czech Republic.

a quantity characterizing the enhancement of the spontaneous emission rate as

$$\xi_{DR} = \frac{\Gamma_{nr} + \Gamma_r F_p}{\Gamma_{nr} + \Gamma_r}. \tag{14}$$

Expression (13) tells us that in the emitter-metal particle system, plasmon modes can affect photoluminescence in the following ways: a) increase the PL intensity by increasing the intensity of the excitation field at plasmonic hot spots; b) increase the PL intensity by increasing the external part of the Purcell factor; c) decrease the PL intensity by increasing the total Purcell factor; if the absorbing part of the Purcell factor increases in this case, then such a process is called PL quenching. These values depend on many parameters including the size of the plasmonic particle, the quantum yield of the fluorophore, the distance between two objects, the spectral overlap of the plasmon resonance of the particle with the absorption/emission spectrum of the fluorophore, the mutual orientation of the emitters and the metal particle, and even the number of emitters associated with the particle [28; 29]. As a result, both a significant increase in [30; 31] and a strong quenching [32; 33] of PL have been experimentally observed in the literature, depending on the specific situation.

To study the ability of the considered gold nanorod to enhance the PL intensity, Purcell factors were calculated for dipoles located in coordinates 1–20 (see Fig. 11a–c), and then the obtained enhancement factors are averaged over the direction and position of the dipole. The resulting enhancement factors are shown in Fig. 11d–g. It can be seen from it that the excitation efficiency of emitters located near the nanorod increases $\approx$2–2.7 times compared to emitters in a homogeneous medium. The PL enhancement also increases monotonically to $\approx$10.5 as the shell thickness decreases to 2 nm. Note that the average PL enhancement factor does not have a local maximum, which is a consequence of the combination of the obtained values of the Purcell factor, the excitation intensity, and the radiative and nonradiative decay rates. The enhancement of the average quantum yield, on the contrary, has a local maximum at a thickness of $h = 5$ nm, reaching the value of $\approx$4.2, which is about 1.7 times greater than for a shell thickness of 20 nm. Finally, the enhancement of the spontaneous emission rate increases monotonically by more than an order of magnitude as the shell thickness decreases from 20 to 2.

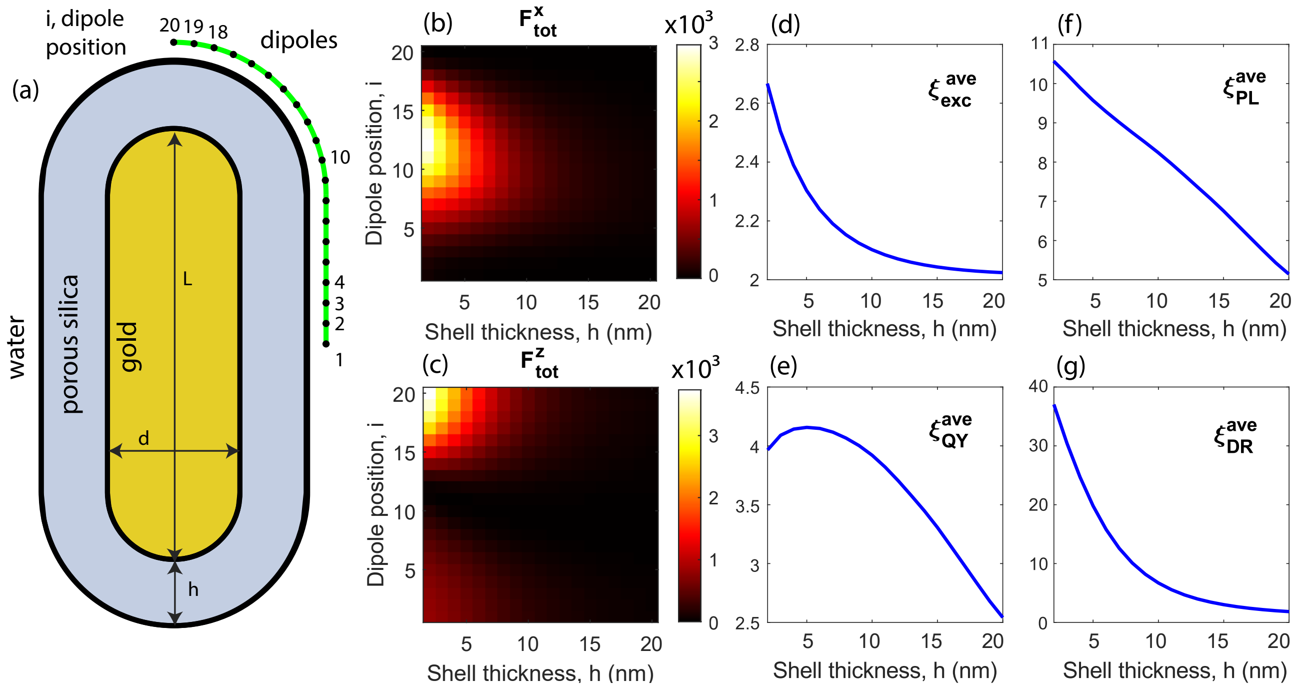

Fig. 11 — (a) Diagram of a gold nanorod and electric dipoles near it. (b) and (c) Total Purcell factor of x- and z-dipoles. (d)–(g) PL excitation enhancement, $\xi^{\text{ave}}_{\text{exc}}$, PL intensity enhancement, $\xi^{\text{ave}}_{\text{PL}}$, PL quantum yield enhancement, $\xi^{\text{ave}}_{\text{QY}}$, and PL decay time enhancement, $\xi^{\text{ave}}_{\text{DR}}$, averaged over the dipole coordinate and direction, as a function of the thickness of the buffer layer h. The calculations were performed for the excitation wavelength $\lambda_{\text{exc}} = 405\,\text{nm}$, the PL wavelength $\lambda_{\text{PL}} = 780\,\text{nm}$, and the nanorod size $L = 65\,\text{nm}$, $d = 18.8\,\text{nm}$, emitter parameters: $\Gamma_r = 3.4\,\text{kHz}$, $\Gamma_{nr} = 80\,\text{kHz}$.

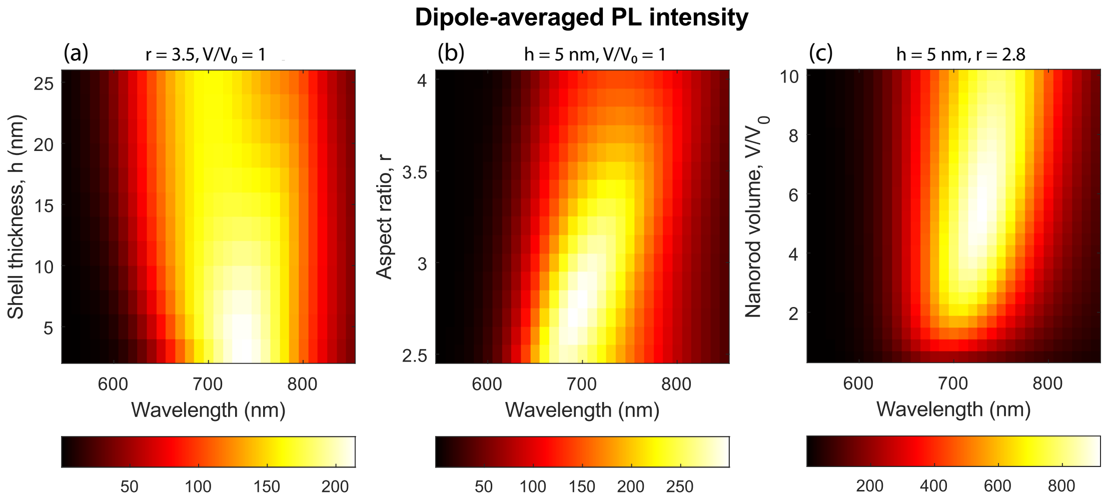

Fig. 12 — Spectrum of the PL intensity averaged over the orientations and coordinates of the dipole as a function of (a) the nanorod shell thickness h, (b) the nanorod aspect ratio $r = L/d$,(c) the volume of the gold part of the nanorod V. In panel (c) the symbol V_0 means the volume of the gold part of the nanorod with $L = 65$ nm, $d = 18.8$ nm. Emitter parameters: $\Gamma_r = 58$ kHz, and Γ_{nr} = 520 kHz. Excitation wavelength $\lambda_{\text{exc}} = 405$ nm.

The dissertation also considers the PL intensities averaged over the orientations and coordinates of the dipole depending on the shell thickness h, the ratio of the length of the nanorod to its diameter $r = L/d$, and the volume of the golden part of the nanorod V. The spectral dependencies of the Purcell factor on h, r, V contain two local maxima: one in the range $\lambda \approx$ 700–850 nm, corresponding to the longitudinal plasmon mode, and the other at the wavelength $\lambda \approx 550$ nm corresponding to the transverse plasmon mode. The shell thickness has almost no effect on the position of the longitudinal plasmon mole, so the position of the maximum of the Purcell factor almost does not change with h. The aspect ratio, on the contrary, strongly affects the plasmonic properties of the nanorod, so the wavelength of the maximum Purcell factor strongly depends on the parameter r. As r decreases, the distance between the local maxima corresponding to the longitudinal and transverse plasmon modes decreases, and for $r = 1$ (the case of a spherical gold nanoparticle) it will become equal to 0, and the wavelength will be, as is known, $\lambda \approx 520$ nm. The calculated PL intensity spectra are shown in Fig. 12d–f. It can be seen, in each of the above dependencies of the PL spectrum there is an optimal value of the corresponding parameter at which the PL intensity reaches a maximum: these are $h \approx 5$ nm, $r \approx 2.8$, $V \approx 6V_0$. These optimal values, as well as the very fact of their presence, as already mentioned, are the result of a combination of the obtained values of the Purcell factor, the excitation intensity, and the rates of radiative and nonradiative recombination.

Section 4.4 considers the Purcell factor of dipoles located in a photonic crystal slab waveguide, which is a silicon waveguide layer with a hexagonal lattice of air pores on a SiO_2 substrate. Interest in such research is due to the fact that so far only cavity-based photonic crystal slabs have been theoretically and experimentally studied in terms of spontaneous emission rate of emitters placed in a cavity, represented by a single unetched or modified pore or in a one-dimensional array of such pores [34—36]. Despite the fact that the Purcell factor for in these structures can be quite large, this method of controlling the rate of spontaneous emission has the disadvantage that it works only for emitters located directly near the resonator mode. Since the physical volume of the resonator is very small, the number of emitters for which the Purcell factor takes large values is also small. On the contrary, in a photonic crystal slab waveguide, emitters located in different unit cells will be in the same conditions, which immediately eliminates the need

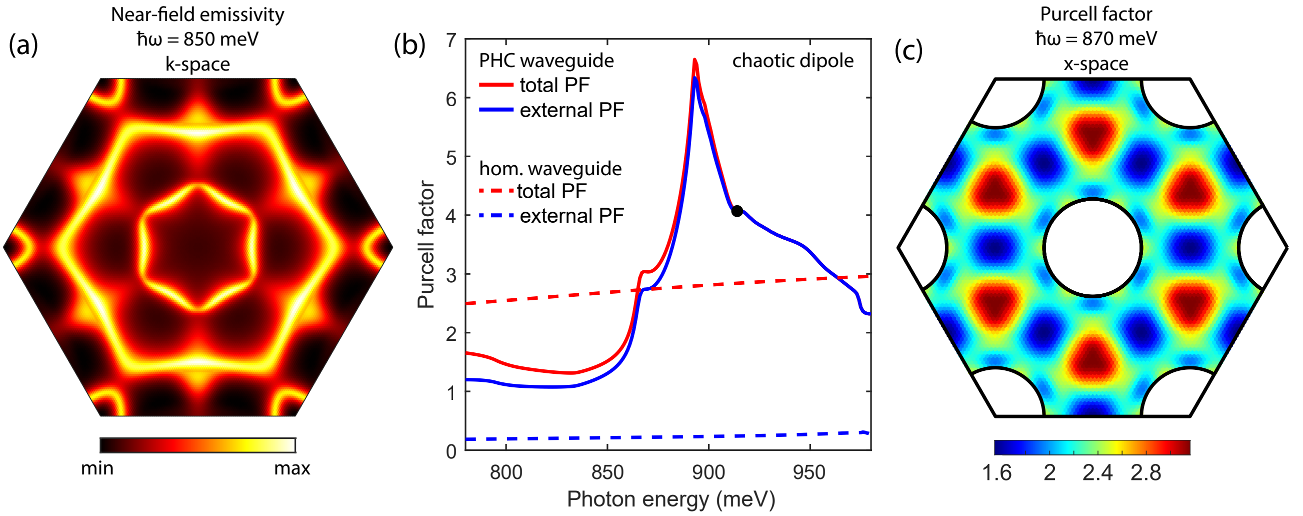

Fig. 13 — (a) Near-field emissivity as a function of the wave vector, averaged over the orientation of the dipoles, inside the first Brillouin zone. Color scale is logarithmic. (b) Spectrum of external and total Purcell factors calculated for PCS and homogeneous waveguides. The black dot denotes the photon energy at which the light cone of the substrate completely covers the first Brillouin zone of the hexagonal PCS grating with the period $a = 625$ nm. (c) Spatial distribution of the Purcell factor on the plane $z = 80$ nm, averaged over the dipole's orienttaion.

to measure the PL signal from a single pore or have a technology for precise positioning of emitters. The calculation of the Purcell factor in a PCS waveguide is also interesting from the point of view of comparing this characteristic with a homogeneous planar waveguide without air pores.

The dependence of the near-field emissivity of the dipole at the most symmetric point of the PCS has a rather complex profile (see Fig. 13a) due to the hybridization of waveguide modes folded into the first Brillouin zone. Integration of this function inside the first Brillouin zone according to formula (10) gives the full Purcell factor. The resulting spectra of the total and external Purcell factor calculated for a homogeneous waveguide layer and a PCS made from it are shown in Fig. 13b. It shows the following facts.

1) In the case of a homogeneous waveguide layer, the total Purcell factor greatly exceeds the external Purcell factor due to the fact that, as is known, radiation outcouples from homogeneous layer only from a small solid angle.

2) The periodicity of the structure greatly increases the external Purcell factor due to the diffraction coupling of the near and far fields, making it almost equal to the total Purcell factor. As the photon energy increases, the light cones of air and the substrate cover an ever larger area in the first Brillouin zone, bringing the value of the external Purcell factor closer and closer to the total Purcell factor.

At a photon energy of $\approx 914\,\text{meV}$, the cross-section of the substrate light cone completely covers the first Brillouin zone of the hexagonal PCS with a period of $a = 625\,\text{nm}$, and then all waveguide modes are coupled to the far field of the substrate, making the external Purcell factor equal to full Purcell factor.

3) The maximum enhancement ($\approx$ 2-fold) of the total Purcell factor due to the periodicity of the structure is achieved at the photon energy $\hbar\omega = 893\,\text{meV}$, at which there are weakly dispersive curves of quasi-waveguide modes.

Finally, the spatial distribution of the Purcell factor for chaotic dipoles inside a PCS cell is shown in Fig. 13c. It can be seen that the Purcell factor for this photon energy takes values from 1.2 to 3.5 depending on the position of the dipole in the structure and its orientation.

In the **fifth chapter**, near-field radiative heat transfer between homogeneous parallel plates of polar materials is studied. In the introductory part of the fifth chapter, a review of the literature on this topic is given, where it is shown that interest in the study of this phenomenon is associated with a multiple increase in the power of radiative heat transfer between two closely spaced bodies compared to the case of two black bodies located in the far field of each other, described by Stephan-Boltzmann's law[37]. The increase in the radiative heat transfer power occurs due to the fact that the evanescent waves corresponding to surface states, such as plasmon-polaritons and phonon-polaritons, do not completely decay at a small distance between objects. Until recently, most theoretical and experimental work has been devoted almost exclusively to stationary radiative heat transfer. However, all systems exchanging thermal energy are characterized by some thermalization time, the study of which is the subject of the fifth chapter.

Section 5.1 describes methods for calculating the spectral radiative heat flux between plates. It is shown that in the most general case of several arbitrary objects, the spectrum of the radiative heat flux at any point of the structure can be found using the fluctuation-dissipation theorem, which describes thermal radiation as a fluctuating electromagnetic field created by the chaotic motion of charged particles inside the body. From a mathematical point of view, this theorem relates the ensemble-averaged spatial correlation function of current densities and the average energy of the Planck oscillator $\Theta(\omega,T)$ [38]. In the classical case, when $k_B T \gg \hbar\omega$, the fluctuation-dissipation theorem can be written as

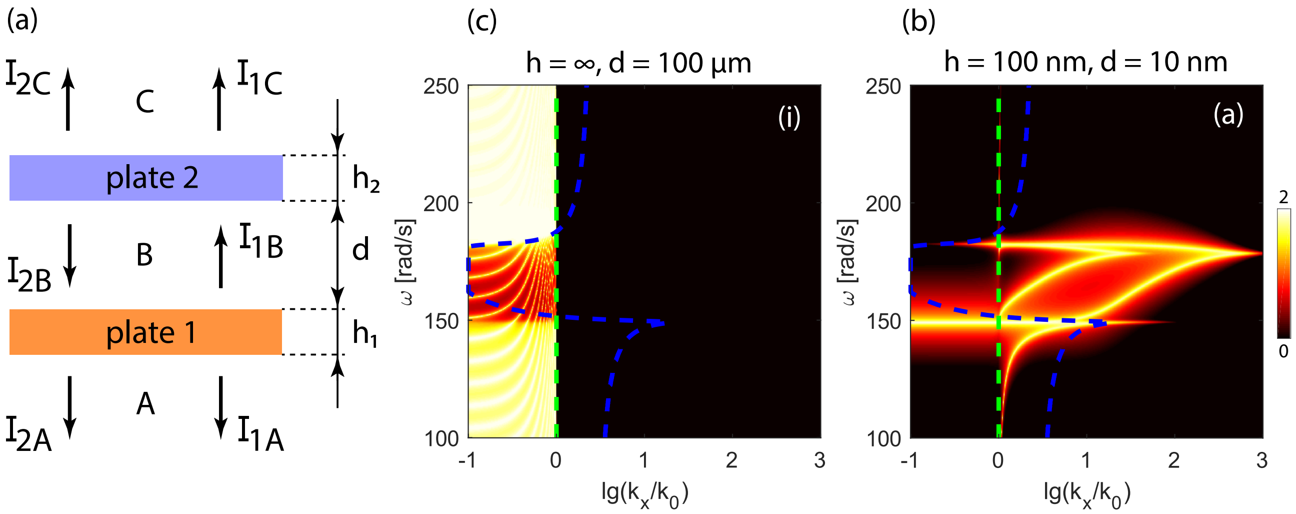

Fig. 14 — (a) Diagram of two parallel plates and thermal radiation fluxes. (b) and (c) Transmittances of $\mathcal{T}_{12}$ (summed over s- and p-polarizations, so the color scale has a maximum value of 2). The green dotted line means the vacuum light cone, the blue dotted line shows the SiC light cone, that is, it corresponds to frequencies and wave vectors such that $\omega/c = k_x/\sqrt{\varepsilon_{\mathrm{SiC}}}$.

$$\langle j_\alpha(\vec{r},\omega) j_\beta(r',\omega)\rangle = \frac{\omega\varepsilon_s''(\omega)}{\pi}\Theta(\omega,T)\delta(\vec{r}-r')\delta(\omega-\omega')\delta_{\alpha\beta}, \tag{15}$$

where $\vec{j}(\vec{r})$ is the current density, ε_s'' is the imaginary part of the dielectric permittivity of the plate material, α and $\beta = x$, y, z, δ is the Dirac function, $\delta_{\alpha\beta}$ is the Kronecker symbol, and the function $\Theta(\omega,T)$ is defined as follows:

$$\Theta(\omega,T) = \frac{\hbar\omega}{\exp(\hbar\omega/k_B T) - 1} \tag{16}$$

where k_B is the Boltzmann constant. The meaning of the fluctuation-dissipation theorem from the viewpoint of modeling thermal radiation is that it connects the thermodynamic part of the problem (average energy of the Planck oscillator) with the electrodynamic part (current density). Therefore, the radiative heat flux from one plate to another can be found using electrodynamics methods for calculating the radiation of oscillating currents [37; 39]. In the case of two homogeneous parallel plates, the total intensity of thermal radiation generated by plate 1 in regions A, B, or C (see diagram in Fig. 14a) is determined as an integral over frequency and wave vector spectral density of the thermal radiation flux:

$$I_{1X} = \frac{1}{2\pi} \int\limits_0^{\infty} \Theta(\omega, T_1) \mathrm{d}\omega \cdot \frac{1}{4\pi^2} \iint\limits_{-\infty}^{+\infty} \sum_{j=s,p} \mathcal{T}_{1X}^{j}(\omega, k_x, k_y) \mathrm{d}k_x \mathrm{d}k_y, \tag{17}$$

where T is the temperature of plate 1, and $\mathcal{T}_{1X}^{j}$ is the transmittance of thermal radiation from plate 1 in polarization state $j = s$ or p to region X = A, B or C, which depends on the frequency ω and the in-plane wave vector. (k_x, k_y) and coefficients can be found by scattering matrix method for s- and p-polarizations. Note that the transmission coefficient $\mathcal{T}_{1B}$ has the meaning of the probability that a thermal photon generated in plate 1 due to thermal fluctuations will reach plate 2 and either be absorbed in it or pass through it and propagate in area A. Similarly, the transmission coefficients $\mathcal{T}_{1A}$ and $\mathcal{T}_{1C}$ are the probabilities that the thermal photon of plate 1 will propagate as a result of multi-reflections from the interfaces in areas A or C.

Section 5.2 studies the problem of heat transfer between two parallel silicon carbide plates with the same thickness h, located at a distance d from each other and surrounded by vacuum in the static and dynamic cases. The choice of silicon carbide as a material is due to the fact that it is characterized by longitudinal and transverse optical phonons in the mid-IR range, which contribute to thermal radiation and near-field radiative heat transfer.

A static study of near-field radiative heat transfer between silicon carbide plates begins with the calculation of the radiation transmittance from plate 1 to plate 2, $\mathcal{T}_{12}$. It is shown that heat exchange between semi-infinite plates located at a large distance from each other occurs inside the vacuum light cone; in this case, the coefficient $\mathcal{T}_{12}$ is suppressed in the Reststrahlen band, within which discrete lines are observed corresponding to Fabry-Perot resonances on the gap size between the plates (Fig. 14b). As the distance between the plates decreases, the continuum of states located under the light cone of silicon carbide start to come into play, so do the phonon-polaritons from the Reststrahlen band. At a small gap between the plates, both of these photonic states begin to contribute to radiative heat transfer which is due to the tunneling of photons from one plate to another on incompletely decayed evanescent waves. When the plates have a finite thickness, the surface phonon-polaritons at the four vacuum/SiC interfaces begin to interact with each other, forming 4 hybrid modes in the Reststrahlen band (Fig. 14c). In addition, the TO phonon always contributes to the radiative heat transfer. It is shown that the indicated features of the transmission coefficient $\mathcal{T}_{12}$ appear as peaks in the spectra of radiative heat transfer between the plates.

The dependencies of the total intensity I_{12} of thermal radiation generated by plate 1 and absorbed by plate 2 on the thickness of the plates and on the distance between the plates are also analyzed. As d decreases, the heat transfer intensity increases as $1/d^2$ for $d < 100\,\text{nm}$. As the distance d increases, the coupling weakens and for $d >$ 30 µm the function $I_{12}(d)$ is constant; this means that for such d only propagating waves contribute to the heat transfer between the plates. This corresponds to Wien's law, which says that in the far-field, the intensity of heat transfer does not depend on the distance between objects. By inspecting the $I_{12}(d)$ profile, one can call the range of distances $d < 100\,\text{nm}$ as a near-field regime, while the range $d > 30\,\mu\text{m}$ as a far-field regime. The dependence of I_{12} on the thickness of the plates is very weak at a small distance between the plates. Consequently, the heat transfer between the plates in the near-field is determined mainly by the radiation and absorption of those parts of SiC plates which are adjacent to the separating vacuum gap. In the far-field regime, at small h, the intensity of heat transfer increases with h, since the thicker the radiating plate, the more thermal energy it radiates. However, when the thickness of the plates h is large enough compared to the wavelength of thermal radiation, the heat transfer intensity reaches a constant value.

To calculate the dynamics of the heat transfer, an integro-differential equation is solved for the temperature $T_2(t)$:

$$\rho_2 C_{v2} h_2 \frac{dT_2(t)}{dt} = I_{1B}(T_1) - I_{2B}(T_2) - I_{1C}(T_1) - I_{2C}(T_2), \tag{18}$$

where C_{v2} is the heat capacity at constant volume of plate 2, modeled by the Debye model, and ρ is its density. It is assumed that the temperature of plate 1 is fixed at 300 K, and the temperature of plate 2 changes with time only due to radiative heat transfer from plate 1. In particular, heat transfer ways such as convection and heat conduction through phonons or electrons are excluded. In the dissertation it is shown that equation (18) is applicable for thicknesses and distances between plates less than 1. The time dependencies of the temperature of

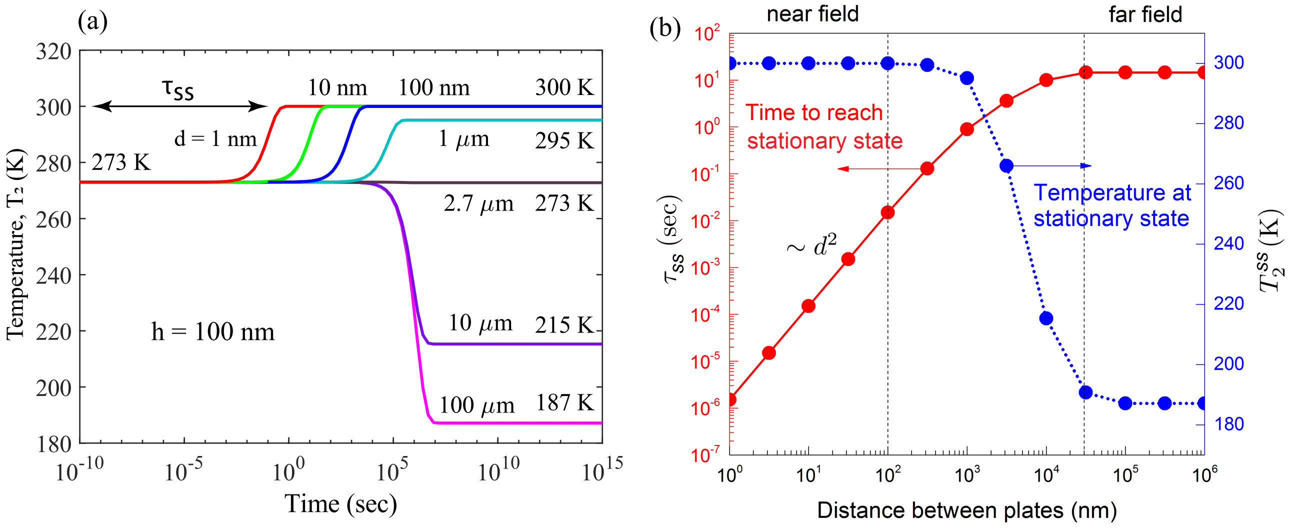

Fig. 15 — (a) Temporal dependencies of the temperature of plate 2, calculated for different distances between the plates d. Plate thickness h =100 nm. (b) Thermalization time of plate 2, τ_{ss}, and the steady-state temperature of plate 2, $T^{ss}{}_2$ as a function of the distance between the plates. Plate thickness $h = 100\,\text{nm}$. $T_1 = 300\,\text{K}$, $T_2(0) = 273\,\text{K}$.

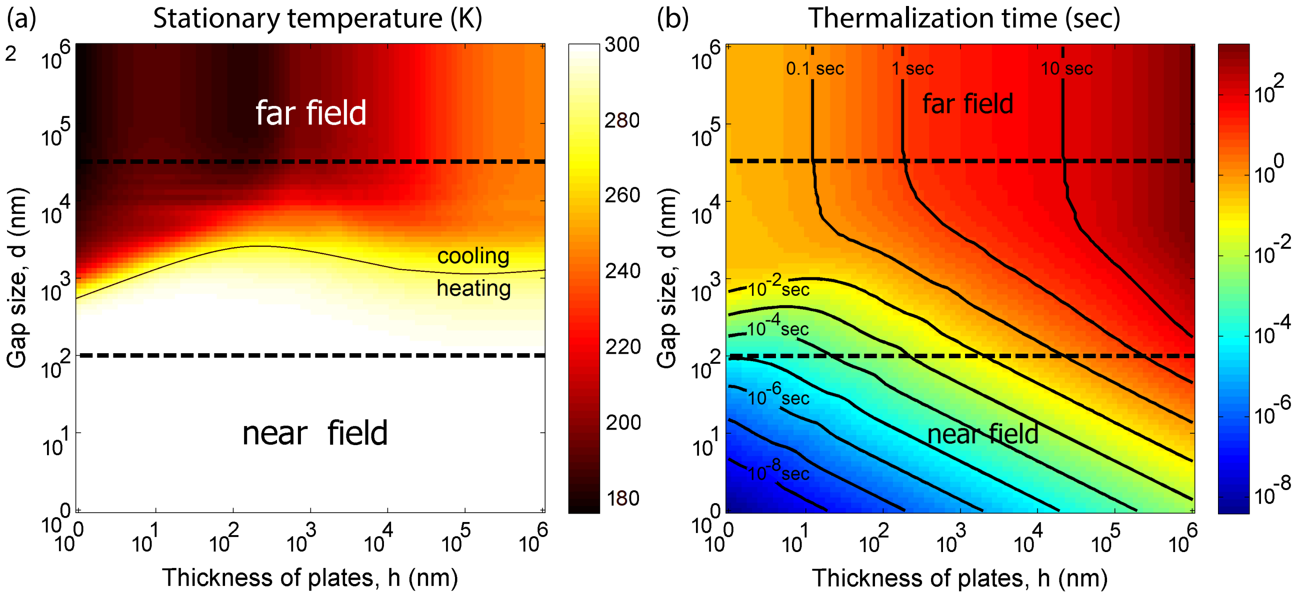

Fig. 16 — Steady-state temperature of plate 2 (a) and thermalization time (b) as two-dimensional functions of the distance between the plates, d, and the thickness of the plates, h. The near- and far-field regimes are separated by black dotted lines. The color scales on the right show the calculated parameter values. The solid line in panel (a) is the contour at $T_2^{ss} = 273$ K, which separates the heating and cooling regimes under the assumption that $T_2(0) = 273\,\text{K}$, $T_1 = 300\,\text{K}$.

plate 2, calculated for different distances between the plates, are shown in Fig. 15a. It can be seen that at small distances $d = 1$, 10 or 100 nm, due to heat exchange with plate 1, plate 2 heats up with time and its temperature saturates at to 300 K.

In the case of $d = 1\,\mu$m, the temperature $T_2(t)$ also increases with time, but does not reach the temperature of plate 1. This is explained by the fact that the heat transfer intensity from plate 1 to plate 2 is not large enough to compensate a decrease in the internal energy of the plate 2 due to its thermal emission into the environment. As the distance d increases, the heat transfer intensity becomes less and less. At $d = 2.7\,\mu\text{m}$, the temperature T_2 no longer changes with time, and at $d < 2.7\,\mu\text{m}$, the temperature of plate 2 decreases.

Fig. 15 shows the dependence of the thermalization time τ_{ss} and the steady-state temperature of plate 2 T^{ss} on the distance between the plates d. When $d < 100\,\text{nm}$ (near-field regime), the thermalization time τ_{ss} is relatively short and increases proportionally to d^2, and the temperature T_2 reaches 300 K. The value of τ_{ss} changes from $1.5\,\mu$s to ≈ 15 ms as the distance d increases from 1 to 100 nm. In the far-field regime ($d > 30\,\mu\text{m}$), the thermalization time and the steady-state temperature do not depend on the distance between the plates and take the values $\tau_{ss} = 14.5\,\text{s}$, $T_2^{ss} = 187\,\text{K}$.

Section 5.2 also considers the quantities T_2^{ss} and τ_{ss} as two-dimensional functions of the plate thickness h and the distance between them d (see Fig. ??). It can be seen that when d is small enough (near-field regime), the heat transfer intensity I_{12} is high, the temperature of plate 2 reaches 300 K, and the thermalization time of plate 2 is proportional to hd^2. In contrast to the near field, in the far-field regime only propagating waves are involved in heat transfer from plate 1 to plate 2, and therefore the temperature of plate 2 in the stationary state is lower than the temperature of the heat source (plate 1). In this case, the thermalization time τ_{ss} does not depend on d, but depends on h. The gap size value, which separates the plate 2 heating and cooling regimes, varies from 560 nm to 2.8 m, depending on the thickness of the plates.

In Section 5.3, the effect of bistability in near-field radiative heat transfer in a system of VO_2 and SiO_2 plates in the near-field regime, when the distance between the plates is small enough for photon tunneling, is studied. The physical basis for obtaining the bistability effect is a first-order phase transition in VO_2 at a temperature $T_{ph} = 340\,\text{K}$ [40]. At $T < T_{ph}$, vanadium dioxide is a uniaxial semiconductor crystal, and at $T > T_{ph}$ it is an amorphous metal. In modeling near-field radiative heat transfer, the hysteresis of optical constants VO_2 is taken into account, and its temperature dependence of the specific heat capacity in constant

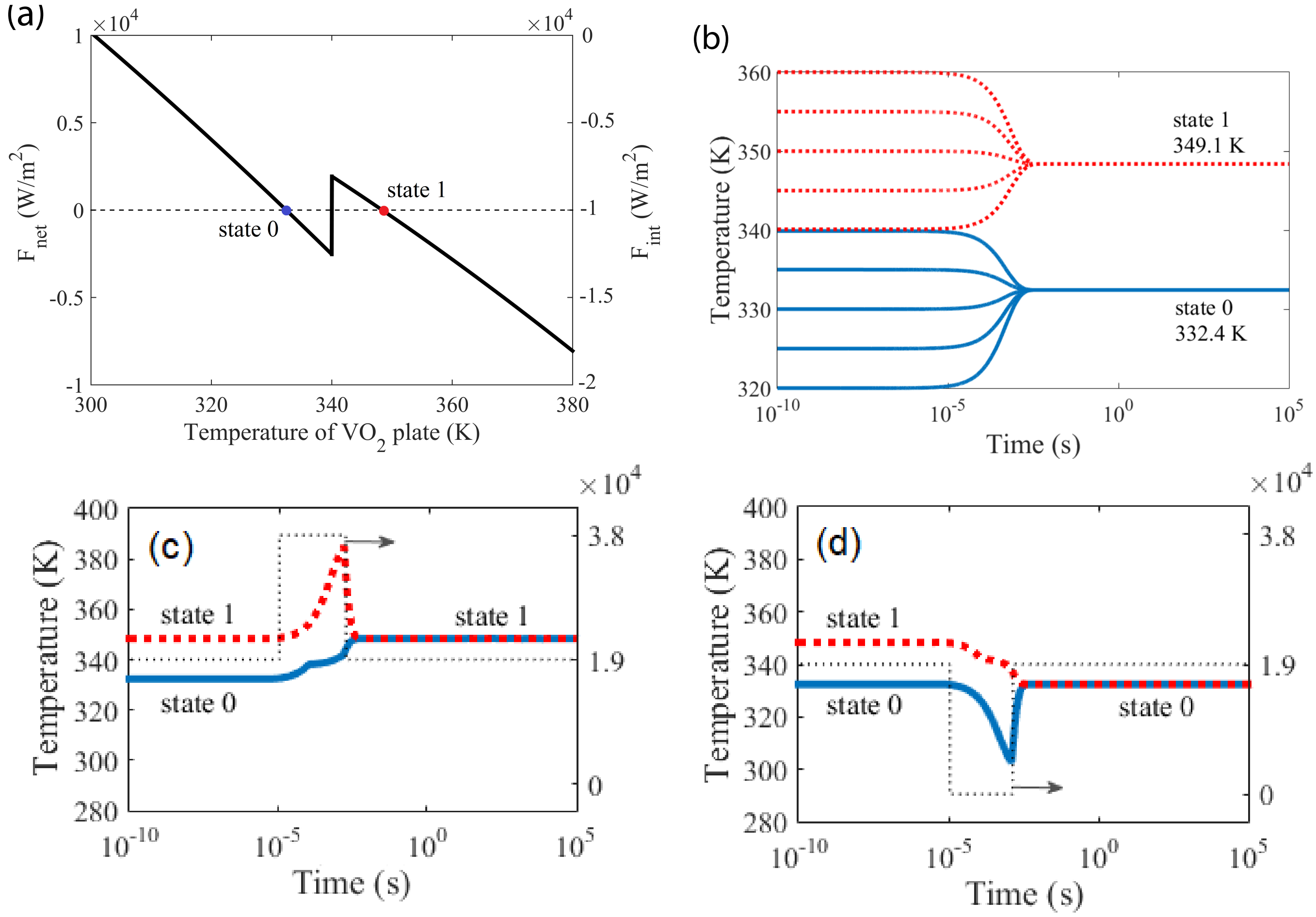

Fig. 17 — (a) Heat transfer power from SiO_2 plate to VO_2 plate, $F_{\text{int}}(T_2)$ and net heat flux $F_{net}(T_2)$ for VO_2 plate as a function of its temperature. (b) Temporal dependencies of the temperature of VO_2 plate at various initial values. (c) and (d) Switching dynamics of the VO_2 plate from state 0 to 1 and vice versa. The dotted lines show the switching pulse of the external source. $h = 50$ nm, $d = 50$ nm, $F_0 = 1.9 \cdot 10^4\,\text{W/m}^2$, T_{SiO_2}=300 K.

volume VO_2 is calculated using the Debye model. In addition, since the metal-insulator transition is characterized by the latent heat of the phase transition, the specific heat at constant volume in the phase transition temperature range $\{T_{ph}-\Delta T, T_{ph}+\Delta T\}$ will have a related additional component: $c_v = c_{vo}+\Delta c_v$ [41]. Here c_{vo} is the heat capacity calculated by the Debye model, and the additional heat capacity Δc_v is chosen such that $2\Delta c_v \Delta T = L$, where $\Delta T = 2$,K and $L = 51.49\,\text{J/g}$. Finally, it is assumed that in the heating or cooling regime, the optical constants VO_2 remain unchanged until the total amount of heat required for the phase transition is absorbed. The choice of SiO_2 as the material of the lower plate is explained by the intersection of the SiO_2 and VO_2 phonon lines and, as a consequence, by the high coefficient of radiative heat transfer between the plates. In calculations, we assume that the temperature of the environment (bath) is $T_{bath} = 300\,\mathrm{K}$, the temperature of the SiO_2 plate is fixed at 300 K, and the temperature of VO_2 varies. In the stationary state, the algebraic sum of the thermal energy fluxes emitted and absorbed by the VO_2 plate is equal to zero. This can be described by the following equation:

$$I_{\mathrm{net}}(T_2) \equiv I_{\mathrm{int}}(T_2) + I_{\mathrm{bath}} + I_{\mathrm{ext}} = 0, \tag{19}$$

where $I_{\mathrm{int}}(T_2) = I_{1B} - I_{1C} - I_{2B} - I_{2C}$ is the heat transfer power from the SiO_2 plate to the VO_2 plate due to the difference in their temperatures. The term I_{bath} denotes the power of absorbed by the plate VO_2 due to thermal radiation of the environment, and can be calculated as $-I_{\mathrm{int}}(T_{\mathrm{bath}})$, and the term I_{ext} is the power absorbed by the VO_2 plate from some external energy source. In practice, the external energy source may be a heat source, a laser, or a heater. At a fixed temperature of the SiO_2 plate with some external power, the function $I_{\mathrm{net}}(T_2)$, which determines the steady-state temperature of the VO_2 plate, can have three roots (see Fig. 17a) due to the strong temperature dependence of the VO_2 dielectric permittivity [42]. Two of these roots correspond to thermal steady states. Since at a sufficiently small distance between the plates the characteristic heat transfer power is several orders of magnitude higher than in the case large distance between the plates, then for a given heat capacity of the plate VO_2 there is a significant reduction in the thermal relaxation time [A15]. Thus, the VO_2 plate has two steady states, which differ in temperature and phase state. Further, the steady state with $T_2 = 332.4\,\mathrm{K}$ will be called state “0”, and with $T_2 = 349.1\,\mathrm{K}$ — state “1”.

To check whether states “0”and “1”are stable in time, the temporal temperature dynamics of the VO_2 plate was simulated using equation (18). The solution of this equation is shown in Fig. 17b for initial plate temperatures VO_2, $T_2(0)$, 320–360. K. It can be seen that when the initial temperature of the VO_2 plate is less than 340 K, the steady-state temperature is 332.4 K. On the other hand, for $T_2(0) > 340\,\mathrm{K}$, the steady-state temperature is 349.1 K. These equilibrium temperatures can be obtained from an analysis of the temperature dependence of the net heat flux for the VO_2 plate (see Fig. 17a). In both cases, the phase state of the VO_2 plate does not change during thermalization. The thermalization time for the VO_2 plate is 3 ms and is determined by the thickness

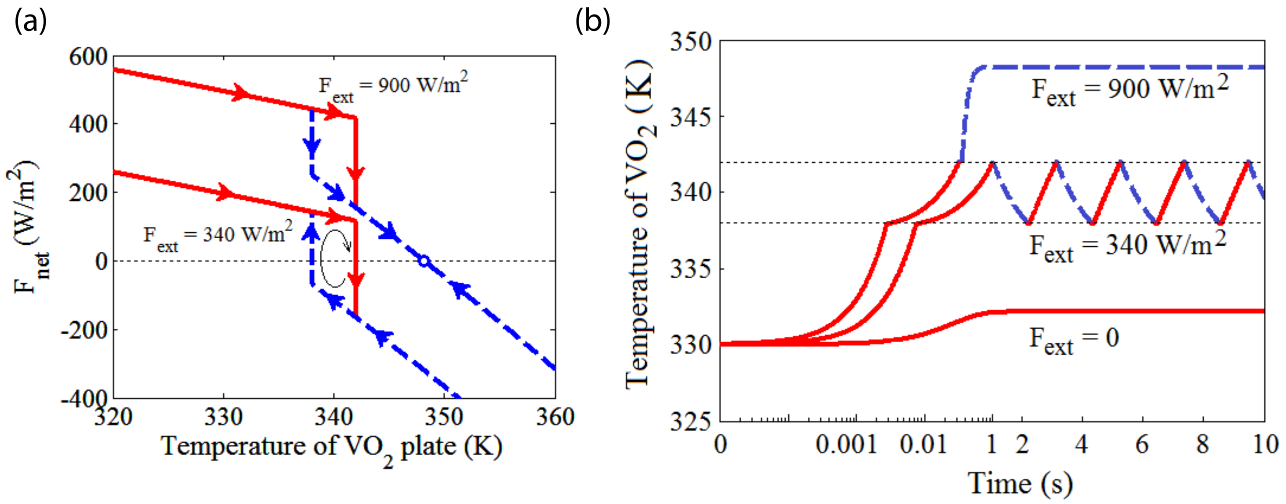

Fig. 18 — (a) Net heat flux I_{net} for the VO_2 plate as a function of its temperature T_2. The arrows show the directions of temperature relaxation. (b) Time evolution of the temperature of the VO_2 plate at various external powers, F_{ext}. The solid (dashed) lines indicate the time intervals when VO_2 is in the crystalline (metal) phase. Vacuum gap $h = 50$ nm, plate thickness VO_2 $d = 500$ nm, laser power $F_0 = 340$ and 900 W/m^2.

of the VO_2 plate h, the distance between the plates d and the characteristics of the material [A15].

Time-varying external power can be used to switch between states “0”and “1”. We will assume that the $I_{\text{ext}}(t)$ function contains a single rectangular pulse Δt with a positive or negative amplitude ΔI. The parameters of the pulses indicated in the text of the dissertation are chosen in such a way that during the time of their action, the change in the temperature of the plate VO_2 is sufficient for a phase transition. As a result, as shown in Fig. 17c,d, regardless of the initial temperature of the VO_2 plate, the system thermalizes to state “1”after exposure to a positive external pulse and to the state “0”after exposure to a negative external pulse. The total time required to switch from state “0”to state “1”is 5 ms, and from state “1”to state “0”— 4 ms. Reducing the switching time is possible only by changing the geometric parameters of the system.

Finally, the phase state of the VO_2 plate can be read by measuring the transmission or reflection spectra of the system. The simulation showed that the transmittance of the entire structure at $\lambda = 1450$nm at normal incidence of the probe beam is 0.43 in the case of the VO_2 crystalline phase and 0.23 in the case of the metallic phase.

In Section 5.4, the effect of self-oscillations in near-field radiative heat transfer is demonstrated for the first time. After the introduction and review of the literature, the dissertation presents a diagram of a self-oscillatory system consisting, as in the previous section, of a semi-infinite SiO_2 plate and a VO_2 plate parallel to it with a thickness of $h = 50\,\mathrm{nm}$, which, according to the near-field mechanism exchange thermal radiation through a vacuum gap. Further, the algebraic sum of the energy fluxes emitted and absorbed by the VO_2 plate is considered as a function of its temperature:

$$I_{\mathrm{net}}(T_2) \equiv I_{\mathrm{int}}(T_2) + I_{\mathrm{ext}} + I_{\mathrm{bath}}. \tag{20}$$

Figure 18a shows the dependence $I_{\mathrm{net}}(T_2)$ for two different powers of the incident laser beam. It can be seen that both dependencies $I_{\mathrm{net}}(T_2)$ have hysteresis, which consists of jumps discontinuities in the total power I_{net} at threshold temperatures $T_{ph} \pm \Delta T$. The directions of T_2 temperature relaxation are determined by the sign of I_{net} and are shown in Fig. 18a by arrows. At the laser beam power $I_{\mathrm{ext}} = 900\,\mathrm{W/m^2}$, the phase trajectory intersects the horizontal axis at a single point $T_2 = 348.1\,\mathrm{K}$. This means that at $I_{\mathrm{ext}} = 900\,\mathrm{W/m^2}$ the system thermalizes to 348.1 K regardless of the initial temperature. In the case of $I_{\mathrm{ext}} = 340\,\mathrm{W/m^2}$, the phase trajectory intersects the horizontal axis at two points, and the directions of temperature relaxation in the metallic and semiconductor phases are opposite. This causes periodic changes in the temperature of the VO_2 plate.

To find the period of self-oscillations, the simulation of the dynamics of radiative heat transfer between the plates was carried out by solving equation (18) with the initial condition $T_2(0) = 330\,\mathrm{K}$. The time dependencies of the temperature $T_2(t)$ obtained for different powers of the laser beam are shown in Fig. 18b. In the absence of an external power flux ($I_{\mathrm{ext}} = 0$), the temperature VO_2 increases to 333 K, and no phase transition occurs. When $I_{\mathrm{ext}} = 900\,\mathrm{W/m^2}$, the VO_2 plate passes from the semiconductor phase to the metallic phase and thermalizes to a constant temperature of 348.1 K, which corresponds to the point of intersection of the phase trajectory with the horizontal axis in Fig. 18. Finally, in the case of a laser power of $340\dot{\mathrm{W}}/\mathrm{m^2}$, the temperature T_2 begins to oscillate after a one-second relaxation to 342 K. The oscillation period is about 2 s, and it is determined by the thermal inertia of the plate VO_2, the distance between the plates, the laser power, the threshold temperatures, and the latent heat of the phase transition. Temperature oscillations are accompanied by periodic switching between phase states VO_2. Note that when the temperature of the plate VO_2 is less than the temperature of the onset of the phase transition (338 K), thermalization occurs faster than in the temperature range 338-342 K. This is due to the fact that in this temperature range, the energy absorbed by the VO_2 plate is spent not only on heating, but also on the phase transition. In calculations, we assumed that the derivatives dn/dT_2 and $d\kappa/dT_2$, are large enough at $T_2 = T_{ph} \pm \Delta T$, which is a key factor in the occurrence of self-oscillations. Additional modeling showed that due to the thermal inertia of the VO_2 plate, self-oscillations can occur even if the parameters $n(T_2)$ and $\kappa(T_2)$ do not change instantly, but in a small temperature range $dT_2 < 1.6$ K near threshold values $T_{ph} \pm \Delta T$.

Since the change in the net heat flux I_{net} with temperature is a process that is essentially non-linear in temperature, which occurs due to a change in the VO_2 internal structure during the phase transition, then the considered self-oscillations belong to self-oscillations of the relaxation type, where the metal-semiconductor phase transition plays the role of positive nonlinear feedback. An oscillatory system never reaches a stationary state, but is constantly thermalized along its phase trajectories.

In the **conclusion** section, the main results of the work are presented:

1. The existing Fourier-modal method in the scattering matrix form has been implemented as programs, which makes it possible to preserve an arbitrary symmetry of two-dimensionally periodic structures when decomposing fields into Fourier harmonics. Based on the implemented algorithm, the reflection, transmission, absorption, photoluminescence, and thermal radiation spectra of various multilayer periodic structures have been calculated, and the dispersion curves of their resonances have been plotted.
2. It has been shown that field redistribution in dielectric and metal-dielectric periodic structures leads to the appearance of quasiguided and hybrid waveguide-plasmon modes, which are diffraction-coupled with the far field and appear as narrow and wide peaks in the reflection and photoluminescence spectra.
3. For the first time, the transverse magneto-optical Kerr effect (TMOKE) in magnetoplasmonic structures with the most common magnetic material on Earth, magnetite, has been studied. A multiple wideband enhancement of the transmission response of TMOKE in such structures

has been demonstrated in comparison with a homogeneous magnetite layer without gold stripes. It has been shown that this effect is due to the hybridization of the waveguide modes of the magnetite layer and the plasmonic modes of the gold grating.

4. The photoluminescence spectra of semiconductor quantum dots in a photonic crystal slab waveguide with a hexagonal lattice have been studied. High-quality peaks have been demonstrated in the photoluminescence spectra of such structures, the existence of which is explained in terms of group theory by symmetry-protected bound states in the continuum. Symmetric field distributions in such modes have been constructed, and their quality factor has been estimated.
5. The emissivity of chiral metasurfaces has been studied. For the first time, an ideal vertical router for the radiation of an oscillating dipole based on a double chiral photonic crystal slab waveguide has been proposed. It has been shown that the principal attainability of 100% of the routing coefficient is due to the D_4-symmetry of the structure and the occurrence of Fano resonances in it. In addition, the possibility of obtaining circularly polarized thermal radiation from such structures in the absence of an external magnetic field has been shown.
6. The Purcell effect of quantum dots located in wedge-shaped layers, in structures with gold nanorods, and also in a photonic crystal slab waveguide has been studied. It has been shown that the redistribution of the eigenfield of these structures significantly affects their Purcell factor. This allows one to determine the internal quantum efficiency of light emitters in wedge-shaped structures, and also leads to the existence of optimal geometric parameters of the system in terms of their photoluminescence intensity. In addition, it has been shown that the periodic structure of a homogeneous photonic crystal slab waveguide does not lead to a significant increase in the Purcell factor of the quantum dots contained in it.
7. The features of near-field radiative heat transfer between homogeneous plates of polar materials in static and dynamic cases have been studied. It has been shown that the intensity of near-field radiative heat transfer between two homogeneous parallel plates, their thermalization time,

as well as their equilibrium temperatures depend significantly on the thickness of the plates and the distance between them. The effects of near-field thermal bistability and thermal self-oscillations in a system of parallel plates of silicon dioxide and vanadium dioxide have been theoretically demonstrated for the first time.

References

1. *Noda S.*, *Fujita M.*, *Asano T.* Spontaneous-emission control by photonic crystals and nanocavities // Nature photonics. — 2007. — т. 1, № 8. — с. 449—458. — URL: http://dx.doi.org/10.1038/nphoton.2007.141.
2. Waveguide-plasmon polaritons: strong coupling of photonic and electronic resonances in a metallic photonic crystal slab / A. Christ [и др.] // Phys. Rev. Lett. — 2003. — т. 91, № 18. — с. 183901. — URL: https://link.aps.org/doi/10.1103/PhysRevLett.91.183901.
3. *Yang D.*, *Ye S.*, *Ge J.* From Metastable Colloidal Crystalline Arrays to Fast Responsive Mechanochromic Photonic Gels: An Organic Gel for Deformation-Based Display Panels // Advanced Functional Materials. — 2014. — т. 24, № 21. — с. 3197—3205.
4. Dynamic modulation of photonic bandgaps in crystalline colloidal arrays under electric field / T. S. Shim [и др.] // Advanced Materials. — 2010. — т. 22, № 40. — с. 4494—4498.
5. Phase change materials and phase change memory / S. Raoux [и др.] // MRS Bulletin. — 2014. — т. 39, № 08. — с. 703—710.
6. *Strelniker Y. M.*, *Bergman D. J.* Strong angular magneto-induced anisotropy of Voigt effect in metal-dielectric metamaterials with periodic nanostructures // Physical Review B. — 2014. — т. 89, № 12. — с. 125312.
7. Near-field magneto-optics and high density data storage / E. Betzig [и др.] // Applied Physics Letters. — 1992. — т. 61, № 2. — с. 142—144.
8. *Gauthier D. J.*, *Narum P.*, *Boyd R. W.* Simple, compact, high-performance permanent-magnet Faraday isolator // Optics letters. — 1986. — т. 11, № 10. — с. 623—625.
9. *Lenz J. E.* A review of magnetic sensors // Proceedings of the IEEE. — 1990. — т. 78, № 6. — с. 973—989.
10. Enhanced transverse magneto-optical Kerr effect in magnetoplasmonic crystals for the design of highly sensitive plasmonic (bio) sensing platforms / B. Diaz-Valencia [и др.] // ACS omega. — 2017. — т. 2, № 11. — с. 7682—7685.
11. *Rotondaro M. D.*, *Zhdanov B. V.*, *Knize R. J.* Generalized treatment of magneto-optical transmission filters // JOSA B. — 2015. — т. 32, № 12. — с. 2507—2513.
12. Magnetoplasmonics and Femtosecond Optomagnetism at the Nanoscale / D. Bossini [и др.] // ACS Photonics. — 2016. — т. 3, № 8. — с. 1385—1400. — DOI: 10.1021/acsphotonics.6b00107.
13. *Sehmi H.*, *Langbein W.*, *Muljarov E.* Optimizing the Drude-Lorentz model for material permittivity: Method, program, and examples for gold, silver, and copper // Physical Review B. — 2017. — т. 95, № 11. — с. 115444.
14. Photonic crystal nanocavity with a Q factor exceeding eleven million / T. Asano [и др.] // Optics express. — 2017. — т. 25, № 3. — с. 1769—1777.

15. Planar photonic crystal cavities with far-field optimization for high coupling efficiency and quality factor / S. L. Portalupi [и др.] // Optics express. — 2010. — т. 18, № 15. — с. 16064—16073.

16. Electromagnetic field structure and normal mode coupling in photonic crystal nanocavities / C. Dineen [и др.] // Optics express. — 2005. — т. 13, № 13. — с. 4980—4985.

17. Bound states in the continuum / C. W. Hsu [и др.] // Nat. Rev. Mater. — 2016. — июль. — т. 1, № 9. — с. 16048. — DOI: 10.1038/natrevmats.2016.48. — URL: http://www.nature.com/articles/natrevmats201648.

18. *Marinica D.*, *Borisov A.*, *Shabanov S.* Bound states in the continuum in photonics // Physical review letters. — 2008. — т. 100, № 18. — с. 183902.

19. *Friedrich H.*, *Wintgen D.* Interfering resonances and bound states in the continuum // Physical Review A. — 1985. — т. 32, № 6. — с. 3231.

20. High-Q states and Strong mode coupling in high-index dielectric resonators. / S. Gladyshev [и др.] // Journal of Physics: Conference Series. т. 1124. — IOP Publishing. 2018. — с. 051058.

21. Optical properties of grooved silicon microstructures: Theory and experiment / S. Dyakov [и др.] // Journal of Experimental and Theoretical Physics. — 2011. — т. 113, № 1. — с. 80—85.

22. *Argyres P. N.* Theory of the Faraday and Kerr effects in ferromagnetics // Physical Review. — 1955. — т. 97, № 2. — с. 334.

23. Discovery of circularly polarized light from a white dwarf / J. C. Kemp [и др.] // The Astrophysical Journal. — 1970. — т. 161. — с. L77.

24. Magnetic-field modulation of the spectrum of coherent thermal radiation of semiconductor layers / O. Kollyukh [и др.] // Physical Review B. — 2005. — т. 71, № 7. — с. 073306.

25. *Menzel C.*, *Rockstuhl C.*, *Lederer F.* Advanced Jones calculus for the classification of periodic metamaterials // Physical Review A. — 2010. — т. 82, № 5. — с. 053811.

26. Circularly polarized light emission from semiconductor planar chiral nanostructures / K. Konishi [и др.] // Physical review letters. — 2011. — т. 106, № 5. — с. 057402.

27. Polarization control of quantum dot emission by chiral photonic crystal slabs / S. V. Lobanov [и др.] // Optics letters. — 2015. — т. 40, № 7. — с. 1528—1531.

28. Plasmon-controlled fluorescence: beyond the intensity enhancement / T. Ming [и др.] // The Journal of Physical Chemistry Letters. — 2012. — т. 3, № 2. — с. 191—202.

29. *Mertens H.*, *Koenderink A.*, *Polman A.* Plasmon-enhanced luminescence near noble-metal nanospheres: Comparison of exact theory and an improved Gersten and Nitzan model // Physical Review B. — 2007. — т. 76, № 11. — с. 115123.

30. Enhancement of single-molecule fluorescence using a gold nanoparticle as an optical nanoantenna / S. Kühn [и др.] // Physical review letters. — 2006. — т. 97, № 1. — с. 017402.

31. Fluorescence enhancement, blinking suppression, and gray states of individual semiconductor nanocrystals close to gold nanoparticles / X. Ma [и др.] // Nano letters. — 2010. — т. 10, № 10. — с. 4166—4174.

32. Distance and wavelength dependent quenching of molecular fluorescence by Au@ SiO2 core–shell nanoparticles / P. Reineck [и др.] // ACS nano. — 2013. — т. 7, № 8. — с. 6636—6648.

33. On the quenching of semiconductor quantum dot photoluminescence by proximal gold nanoparticles / T. Pons [и др.] // Nano letters. — 2007. — т. 7, № 10. — с. 3157—3164.

34. Ultrahigh Purcell factor in photonic crystal slab microcavities / L. Sanchis [и др.] // Physical Review B. — 2007. — т. 76, № 4. — с. 045118.

35. Purcell effect in photonic crystal microcavities embedding InAs/InP quantum wires / J. Canet-Ferrer [и др.] // Optics Express. — 2012. — т. 20, № 7. — с. 7901—7914.

36. *Iwase H.*, *Englund D.*, *Vučković J.* Analysis of the Purcell effect in photonic and plasmonic crystals with losses // Optics express. — 2010. — т. 18, № 16. — с. 16546—16560.

37. Surface electromagnetic waves thermally excited: Radiative heat transfer, coherence properties and Casimir forces revisited in the near field / K. Joulain [и др.] // Surface Science Reports. — 2005. — т. 57, № 3. — с. 59—112.

38. *Ландау Л. Д.*, *Питаевский Л. П.*, *Лифшиц Е. М.* Статистическая физика. — Наука, 1976.

39. *Francoeur M.*, *Pinar Mengüç M.* Role of fluctuational electrodynamics in near-field radiative heat transfer // J. Quant. Spectrosc. Radiat. Transf. — 2008. — т. 109, № 2. — с. 280—293.

40. Mott transition in VO_2 revealed by infrared spectroscopy and nano-imaging / M. M. Qazilbash [и др.] // Science. — 2007. — т. 318, № 5857. — с. 1750—1753.

41. *Berglund C.*, *Guggenheim H.* Electronic Properties of VO_2 near the Semiconductor-Metal Transition // Phys. Rev. — 1969. — т. 185, № 3. — с. 1022.

42. *Zhu L.*, *Otey C. R.*, *Fan S.* Negative differential thermal conductance through vacuum // Appl. Phys. Lett. — 2012. — т. 100, № 4. — с. 044104.

List of author's first tier publications

A1. Photonic Bound States in the Continuum in Si Structures with the Self-Assembled Ge Nanoislands / S. A. Dyakov [и др.] // Laser & Photonics Reviews. — 2021. — с. 2000242. — DOI: `10.1002/lpor.202000242`. — **Selected for the journal Cover image in July**.

A2. Luminescent properties of spatially ordered Ge/Si quantum dots epitaxially grown on a pit-patterned "silicon-on-insulator" substrate / Z. V. Smagina [и др.] // Journal of Luminescence. — 2022. — с. 119033. — DOI: `10.1016/j.jlumin.2022.119033`.

A3. Eigenmode analysis of the waveguide-plasmon structure based on a-Si1-xCx: H layer with 1D gold grating / S. I. Pavlov [и др.] // Photonics and Nanostructures-Fundamentals and Applications. — 2022. — т. 48. — с. 100975. — DOI: `10.1016/j.photonics.2021.100975`.

A4. Optimizing plasmon enhanced luminescence in silicon nanocrystals by gold nanorods / O. Pavelka [и др.] // Nanoscale. — 2021. — т. 13, № 9. — с. 5045—5057. — DOI: `10.1039/D1NR00058F`.

A5. Wide-band enhancement of the transverse magneto-optical Kerr effect in magnetite-based plasmonic crystals / S. Dyakov [и др.] // Physical Review B. — 2019. — т. 100, № 21. — с. 214411. — DOI: `10.1103/PhysRevB.100.214411`.

A6. Quasiguided modes of opaline photonic crystals covered by $\mathrm{Ge}_2 Sb_2 Te_5$ / S. A. Dyakov [и др.] // Physical Review B. — 2017. — т. 96, № 4. — с. 45426. — DOI: `10.1103/PhysRevB.96.045426`.

A7. One-stage formation of two-dimensional photonic crystal and spatially ordered arrays of self-assembled Ge(Si) nanoislands on pit-patterned silicon-on-insulator substrate / A. V. Novikov [и др.] // Nanomaterials. — 2021. — т. 11, № 4. — с. 909. — DOI: `10.3390/nano11040909`.

A8. Vertical Routing of Spinning-Dipole Radiation from a Chiral Metasurface / S. A. Dyakov [и др.] // Physical Review Applied. — 2020. — т. 14, № 2. — с. 024090. — DOI: `10.1103/PhysRevApplied.14.024090`.

A9. Nearly perfect near-infrared luminescence efficiency of Si nanocrystals: A comprehensive quantum yield study employing the Purcell effect / J. Valenta [и др.] // Scientific Reports. — 2019. — т. 9, № 1. — DOI: `10.1038/s41598-019-47825-x`.

A10. Magnetic field free circularly polarized thermal emission from a chiral metasurface / S. A. Dyakov [и др.] // Physical Review B. — 2018. — дек. — т. 98, № 23. — с. 235416. — DOI: `10.1103/PhysRevB.98.235416`.

A11. Plasmon induced modification of silicon nanocrystals photoluminescence in presence of gold nanostripes / S. A. Dyakov [и др.] // Scientific Reports. — 2018. — т. 8, № 1. — с. 4911. — DOI: `10.1038/s41598-018-22633-x`.

A12. Optical properties of silicon nanocrystals covered by periodic array of gold nanowires / S. A. Dyakov [и др.] // Physical Review B. — 2016. — т. 93, № 20. — с. 205413. — DOI: `10.1103/PhysRevB.93.205413`.

A13. Thermal self-oscillations in radiative heat exchange / S. A. Dyakov [и др.] // Applied Physics Letters. — 2015. — февр. — т. 106, № 6. — с. 064103. — DOI: `10.1063/1.4908188`.

A14. Near-field thermal memory based on radiative phase bistability of VO_2 / S. A. Dyakov [и др.] // Journal of Physics D: Applied Physics. — 2015. — т. 48. — с. 305104. — DOI: `10.1088/0022-3727/48/30/305104`.

A15. Thermal radiation dynamics in two parallel plates: The role of near field / S. A. Dyakov [и др.] // Physical Review B - Condensed Matter and Materials Physics. — 2014. — т. 90, № 4. — с. 45414. — DOI: `10.1103/PhysRevB.90.045414`.

List of author's second tier publications

B1. Transverse magneto-optical kerr effect in magnetite covered by array of gold nanostripes / S. Dyakov [и др.] // Semiconductors. — 2018. — т. 52, № 14. — с. 1857—1860. — DOI: `10.1134/S1063782618140099`.

B2. Зависимость люминесцентных свойств упорядоченных групп Ge (Si) наноостровков от параметров ямок на структурированной поверхности подложки "кремний на изоляторе" / Ж. В. Смагина [и др.] // Физика и техника полупроводников. — 2021. — т. 55, № 12. — с. 1210—1215. — DOI: `10.21883/FTP.2021.12.51707.9722`.

B3. Enhancement of the Luminescence Signal from Self-Assembled Ge (Si) Nanoislands due to Interaction with the Modes of Two-Dimensional Photonic Crystals / D. V. Yurasov [и др.] // Semiconductors. — 2020. — т. 54, № 8. — с. 975—981. — DOI: `10.1134/S1063782620080254`.

List of author's publications not included in the dissertation

C1. Resonant mode approximation of the scattering matrix of photonic crystal slabs near several Wood-Rayleigh anomalies / D. Gromyko [и др.] // Photonics and Nanostructures-Fundamentals and Applications. — 2022. — с. 101015. — DOI: `10.1016/j.photonics.2022.101015`.

C2. Strong Local Field Enhancement of Raman Scattering Observed in Metal-Dielectric Gratings due to Vertical Fabry-Perot Modes of Surface Plasmon Polaritons / D. A. Gromyko [и др.] // Physical Review Applied. — 2022. — т. 17, № 2. — с. 024015. — DOI: `10.1103/PhysRevApplied.17.024015`.

C3. Laser Ablated Nanocrystalline Diamond Membrane for Infrared Applications / M. S. Komlenok [и др.] // Sensors. — 2022. — т. 22, № 3. — с. 829. — DOI: `10.3390/s22030829`.

C4. Surface-Enhanced Raman Scattering-Active Gold-Decorated Silicon Nanowire Substrates for Label-Free Detection of Bilirubin / A. D. Kartashova [и др.] // ACS Biomaterials Science & Engineering. — 2021. — DOI: `10.1021/acsbiomaterials.1c00728`.

C5. Enhancing the photoluminescence response of thick Ge-on-Si layers using photonic crystals / D. Yurasov [и др.] // Journal of Physics D: Applied Physics. — 2021. — т. 55, № 7. — с. 075107. — DOI: `10.1088/1361-6463/ac32fe`.

C6. Fourier modal method for Moiré lattices / N. S. Salakhova [и др.] // Physical Review B. — 2021. — т. 104, № 8. — с. 085424. — DOI: `10.1103/PhysRevB.104.085424`.

C7. Dimensional confinement and waveguide effect of Dyakonov surface waves in twisted confined media / D. A. Chermoshentsev [и др.] // Nanophotonics. — 2020. — т. 9, № 16. — с. 4785—4797. — DOI: `10.1515/nanoph-2020-0459`.

C8. Gold nanoparticle-carbon nanotube multilayers on silica microspheres: Optoacoustic-Raman enhancement and potential biomedical applications / D. Nozdriukhin [и др.] // Materials Science and Engineering: C. — 2021. — т. 120. — с. 111736. — DOI: `10.1016/j.msec.2020.111736`.

C9. Fourier-Imaging Spectroscopy of Two-Dimensional Gold Nanodisk Array on Photoluminescent Layer / S. I. Pavlov [и др.] // Semiconductors. — 2020. — т. 54, № 14. — с. 1893—1896. — DOI: `10.1134/S1063782620140225`.

C10. Stimuli-Responsive Microarray Films for Real-Time Sensing of Surrounding Media, Temperature, and Solution Properties via Diffraction Patterns / J. Zhang [и др.] // ACS Applied Materials & Interfaces. — 2020. — т. 12, № 16. — с. 19080—19091. — DOI: `10.1021/acsami.0c05349`.

C11. Gold nanoflowers grown in a porous Si/SiO2 matrix: The fabrication process and plasmonic properties / L. A. Osminkina [и др.] // Applied Surface Science. — 2020. — т. 507. — с. 144989. — DOI: `10.1016/j.apsusc.2019.144989`.

C12. *Fradkin I. M.*, *Dyakov S. A.*, *Gippius N. A.* Nanoparticle lattices with bases: Fourier modal method and dipole approximation // Phys. Rev. B. — 2020. — июль. — т. 102, вып. 4. — с. 045432. — DOI: `10.1103/PhysRevB.102.045432`.

C13. *Fradkin I. M.*, *Dyakov S. A.*, *Gippius N. A.* Thickness-Independent Narrow Resonance in a Stack of Plasmonic Lattices // Physical Review Applied. — 2020. — т. 14, № 5. — с. 054030. — DOI: `10.1103/PhysRevApplied.14.054030`.

C14. Dyakonov-like waveguide modes in an interfacial strip waveguide / E. V. Anikin [и др.] // Physical Review B, Rapid Communications, — 2020. — т. 102, № 16. — с. 161113. — DOI: `10.1103/PhysRevB.102.161113`.

C15. Raman Signal Enhancement Tunable by Gold-Covered Porous Silicon Films with Different Morphology / S. N. Agafilushkina [и др.] // Sensors. — 2020. — т. 20, № 19. — с. 5634. — DOI: `10.1063/1.4884839`.

C16. Single-walled carbon nanotube membranes as non-reflective substrates for nanophotonic applications / D. M. Zhigunov [и др.] // Nanotechnology. — 2020. — т. 32, № 9. — с. 095206. — DOI: `10.1088/1361-6528/abcacc`.

C17. *Fradkin I. M.*, *Dyakov S. A.*, *Gippius N. A.* Fourier modal method for the description of nanoparticle lattices in the dipole approximation // Physical Review B. — 2019. — т. 99, № 7. — с. 75310. — DOI: `10.1103/PhysRevB.99.075310`.

C18. Midinfrared Surface Plasmons in Carbon Nanotube Plasmonic Metasurface / B. I. Afinogenov [и др.] // Physical Review Applied. — 2018. — т. 9, № 2. — с. 24027. — DOI: `10.1103/PhysRevApplied.9.024027`.

C19. Dynamic in-situ sensing of fluid-dispersed 2D materials integrated on microfluidic Si chip / B. T. Hogan [и др.] // Scientific Reports. — 2017. — т. 7. — с. 42120. — DOI: `10.1038/srep42120`.

C20. Near-field radiative heat transfer between metasurfaces: A full-wave study based on two-dimensional grooved metal plates / J. Dai [и др.] // Physical Review B. — 2016. — т. 94, № 12. — с. 125431. — DOI: `10.1103/PhysRevB.94.125431`.

C21. *Dai J.*, *Dyakov S. A.*, *Yan M.* Radiative heat transfer between two dielectric-filled metal gratings // Physical Review B. — 2016. — т. 93, № 15. — с. 155403. — DOI: `10.1103/PhysRevB.93.155403`.

C22. *Dai J.*, *Dyakov S. A.*, *Yan M.* Enhanced near-field radiative heat transfer between corrugated metal plates: Role of spoof surface plasmon polaritons // Physical Review B - Condensed Matter and Materials Physics. — 2015. — т. 92, № 3. — с. 35419. — DOI: `10.1103/PhysRevB.92.035419`.

C23. Absorption and emission of silicon nanocrystals embedded in SiC: Eliminating Fabry-Pérot interference / M. Schnabel [и др.] // Journal of Applied Physics. — 2015. — т. 117, № 4. — с. 45307. — DOI: `10.1063/1.4905671`.

C24. Optical Spectra of Composite One-Dimensional Photonic Crystals with Extended Stop Bands Based on a Si-Air Structure / V. A. Tolmachev [и др.] // Journal of Lightwave Technology. — 2015. — т. 33, № 17. — с. 3577—3583. — DOI: `10.1109/JLT.2015.2444356`.

C25. Absence of quantum confinement effects in the photoluminescence of Si 3N4-embedded Si nanocrystals / D. Hiller [и др.] // Journal of Applied Physics. — 2014. — т. 115, № 20. — с. 204301. — DOI: `10.1063/1.4878699`.

C26. Multi-resonator structure based on continuous silver thin films for transparent conductors / R. Soltanmoradi [и др.] // Applied Physics Letters. — 2014. — т. 105, № 6. — с. 61110. — DOI: `10.1063/1.4893144`.

C27. Silicon nanocrystals in SiNx/SiO2 hetero-superlattices: The loss of size control after thermal annealing / A. Zelenina [и др.] // Journal of Applied Physics. — 2014. — т. 115, № 24. — с. 244304. — DOI: `10.1063/1.4884839`.

C28. Structural and optical properties of size controlled Si nanocrystals in Si3N4 matrix: The nature of photoluminescence peak shift / A. Zelenina [и др.] // Journal of Applied Physics. — 2013. — т. 114, № 18. — с. 184311. — DOI: `10.1063/1.4830026`.

List of invited presentations at international conferences

D1. *Dyakov S. A.* Dyakonov surface waves revisited: waveguide effect and negative anisotropy // Program of VI International Conference on Metamaterials and Nanophotonics METANANO. — online, 13–17 Sept.2021.

D2. *Dyakov S. A.* Optical resonances and the Purcell effect in structures with self-organizing Ge nanoislands // Book of abstracts of XXV symposium Nanophysics and nanoelectronics. — online, 03.2021.

D3. On the fundamental limits of luminescence quantum yield of light-emitting Si nanostructures: What is behind the green catastrophe? / J. Valenta [и др.] // Program of EMRS Fall Meeting. — Warsaw, Poland, 18–21 September.2017.

D4. Plasmonic enhancement of silicon nanocrystals photoluminescence in the presence of gold nanowires / S. A. Dyakov [и др.] // Program of 9th Russian-French Workshop on Nanosciences and Nanotechnologies. — Suzdal, Russia, 3–7 October.2017.

D5. Optical properties of silicon nanocrystals covered by periodic array of gold nanowires / S. A. Dyakov [и др.] // Program of BIT's 4th Annual World Congress of Smart Materials. — Osaka, Japan, 6–8 March 2018.2018.

D6. *Dyakov S. A.* Optical Properties of Silicon nanocrystals covered by periodic array of gold nanowires // Programme of the II international symposium "Advanced studies in the field of chemistry and biomedicine". — Tomsk, Russia, 4–8 June.2018.

D7. *Dyakov S. A.*, *Gippius N. A.*, *Tikhodeev S. G.* Infrared metasurfaces for polarization control of thermal emission // Book of abstracts of 10th Russian-French Workshop on Nanowires and Nanotechnologies. — Clermont-Ferrand, France, 2019.

D8. *Dyakov S.* High quality optical resonances in periodic structures with Si-Ge quantum dots // Book of abstracts of XXIV symposium Nanophysics and nanoelectronics. — Institute of physics of microstructures, RAS. Nizhny Novgorod, 2020.

D9. Near-field thermal memory device / M. Qiu [и др.] // Technical programme of SPIE Optics+Optoelectronics Symposia. — SPIE. Prague, Czech Republic, 13–16 April.2015. — с. 14.

D10. Thermal self-oscillations in radiative heat exchange / S. A. Dyakov [и др.] // Conference programme of the 6th International Conference on Metamaterials, Photonic Crystals and Plasmonics. — City College of New York, New York City, NY, USA, 04–07 August.2015.

D11. Interference enhancement of photoluminescence signal from thin layers with silicon nanocrystals / S. A. Dyakov [и др.] // Proceedings of the Microscopical Society of Ireland Symposium. Program and Abstracts. — University College Cork. Cork, Ireland, 29–31 August.2012. — с. 58. — **Best oral presentation award**.